

**Flux-flow instability across Berezinskii Kosterlitz Thouless phase transition  
in  $\text{KTaO}_3$  (111) based superconductor**

Shashank Kumar Ojha,<sup>1,\*</sup> Prithwijit Mandal,<sup>1,†</sup> Siddharth

Kumar,<sup>1</sup> Jyotirmay Maity,<sup>1</sup> and Srimanta Middey<sup>1,‡</sup>

<sup>1</sup>*Department of Physics, Indian Institute of Science, Bengaluru 560012, India*

arXiv:2206.10361v2 [cond-mat.supr-con] 6 Jun 2023

# Abstract

Abstract: The nature of energy dissipation in 2D superconductors under perpendicular magnetic field at small current excitations has been extensively studied over the past two decades. However, dissipation mechanisms at high current drives remain largely unexplored. Here we report on the distinct behavior of energy dissipation in the  $\text{AlO}_x/\text{KTaO}_3$  (111) system hosting 2D superconductivity in the intermediate disorder regime. The results show that below the Berezinskii Kosterlitz Thouless (BKT) phase transition temperature ( $T_{\text{BKT}}$ ), hot-spots and Larkin Ovchinnikov type flux-flow instability (FFI) are the major channels of dissipation, leading to pronounced voltage instability at large currents. Furthermore, such FFI leads to a rare observation of clockwise hysteresis in current-voltage characteristics within the temperature range  $T_{\text{BKT}} < T < T_C$  ( $T_C$  is superconducting transition temperature). These findings deepen our understanding of how a BKT system ultimately transforms to a normal state under increasing current.

## INTRODUCTION

The ability to conduct dissipationless electrical current is one of the most striking features of a superconductor [1]. The phenomena of pair breaking puts an upper theoretical bound on the maximum current that a superconductor can withstand without dissipation [2]. However, a finite dissipation always sets in at much lower current densities in reality, leading to breakdown of the superconductivity (SC) much before the pair breaking limit is reached. Therefore understanding dissipation mechanism is not only critical to answering some of the fundamental questions about the nature and origin of superconductivity, but will also be pivotal in realizing next generation applications such as superconducting digital memory, cavities for particle accelerators and THz radiation sources etc. [3–6].

In 1D, phase slip centers are the primary cause of dissipation [1]. In 2D, an additional complication arises due to occurrence of a topological phase transition which belongs to the Berezinskii Kosterlitz Thouless (BKT) universality class [7, 8]. Below the BKT phase transition temperature ( $T_{\text{BKT}}$ ), bound vortex-antivortex pairs are the bare topological excitations which become unbound above the  $T_{\text{BKT}}$  [8–11]. Nonetheless, some bound vortex-antivortex pairs still exist even in the temperature range  $T_{\text{BKT}} \leq T \leq T_C$  under zero electrical current ( $I$ ) [12]. Application of

---

\* Contributed equally; [shashank@iisc.ac.in](mailto:shashank@iisc.ac.in)

† Contributed equally

‡ [smiddey@iisc.ac.in](mailto:smiddey@iisc.ac.in)

$I$  leads to a further increase in free vortex density due to unbinding of bound vortex-antivortex pairs. These free vortices feel magnus force under the applied current and hence can move with very high velocities at large currents [3]. While the presence of ultra-fast moving vortices and its possible connection with phase slip lines (which are 2D analogue of phase slip centers) has been demonstrated earlier [13–17], what happens to these topological defects just before the breakdown remains puzzling. One of the proposition has been that such fast moving vortices can become unstable at large currents leading to flux-flow instability (FFI) as proposed by Larkin and Ovchinnikov (LO) [18, 19]. While such a scenario has been demonstrated under magnetic field [3, 19–27], its manifestation in BKT systems in absence of external magnetic field remains scarce [28].

The presence of disorder in samples, which is inevitable in reality, further complicates this problem by turning the BKT system inhomogeneous. Such inhomogeneities might range from atomic level point defects to macroscopically phase separated regions [29–32]. While the former determines the vortex pinning strength, the latter often leads to a network of superconducting puddles joined by weak superconducting links. Such weak links, which are hosts of hot-spots, are very fragile under large electric field and are another competing source of dissipation under large current in the absence of magnetic field [33]. In the past, much of the attention has been paid to understanding the dissipation in either very clean or dirty system. Notably, all of these measurements have been primarily performed in the presence of magnetic field (under very small  $I$ ) and very little is known about the nature of dissipation under large current [16, 28, 34]. Further, what happens in the intermediate disordered regime also remains an open question.

In recent years, oxide heterostructure based interfacial superconductors have turned out to a potential platform for understanding SC in 2D limit and the focus has been primarily on SrTiO<sub>3</sub> (STO) based systems [35–38]. Recently, SC has been discovered at the interface and surface of (111) oriented KTaO<sub>3</sub> (KTO) (see Fig. 1a) with  $T_C \sim 1.5\text{-}2.2$  K [39–42]. The  $T_C$  is one order of magnitude higher than heavily investigated STO based heterostructure [35, 43] and hence has generated tremendous excitement in the field of interfacial SC. Interestingly, SC was also found to be strongly influenced by the choice of over-layer grown on KTO (111) substrate. For example, the presence of a magnetic element in the overlayer could lead to a stripe order near superconducting transition [39]. While the current focus is on understanding the origin of higher  $T_C$  [44] and possible role of spin-orbit coupling (SOC), the nature of dissipation at large current drive remains completely unknown in KTO based systems. Surprisingly, this issue also remains unexplored for any oxide based interfacial superconductors.

In this work, we investigate the underlying mechanisms that cause dissipation at high current drives in KTO (111) based interfacial superconductor. Through a combination of thorough transport measurements and analysis, we have identified strong indications of LO type FFI in association with Joule heating effects. While such a behavior had previously been observed in type II superconductors under the influence of a magnetic field [3, 19–27], experimental evidence of such instabilities in the absence of an external magnetic field has remained elusive until now.

## RESULTS

**Two-dimensional superconductivity in  $\text{AlO}_x/\text{KTaO}_3$  (111) with intermediate disorder:** In order to avoid the potential complications caused by a magnetic overlayer on the nature of dissipation, we have fabricated a new superconducting interface by ablating non-magnetic  $\text{Al}_2\text{O}_3$  on KTO (111) substrate [dimension  $5 \text{ mm} \times 5 \text{ mm} \times 0.5 \text{ mm}$ ] by pulsed laser deposition technique (see Methods, Supplementary Note 1 and Supplementary Fig. 1). The resultant film is amorphous. For electrical transport measurements, two Hall bars were patterned along two inequivalent crystallographic directions :  $[11\bar{2}]$  and  $[1\bar{1}0]$  (Fig. 1b) by selective scratching of film deep into the substrate [45]. Fig. 1c shows the sheet resistance ( $R_S$ ) vs. temperature plot of a 7 nm  $\text{AlO}_x/\text{KTO}$  (111) sample. As evident, the interface exhibits metallic behavior down to low temperature confirming the formation of two dimensional electron gas (2DEG). The origin of the 2DEG is connected to the creation of oxygen vacancies (OVs) [42, 46] within the top few layers of the KTO substrate. Further, a clear superconducting transition is observed with negligible anisotropy e.g.  $T_C = 1.55 \text{ K}$  and  $1.51 \text{ K}$  for current driven along  $[11\bar{2}]$  and  $[1\bar{1}0]$  respectively (inset of Fig. 1c) ( $T_C$  is estimated from the condition  $R_S(T_C) = 0.5 \times R_S(5 \text{ K})$ ). While the value of  $T_C$  is very similar to the previous reports [39, 40], the observation of little anisotropy is in sharp contrast with the report of large in-plane anisotropy for  $\text{EuO}/\text{KTO}$  (111) near the superconducting transition,  $T_C$  [39].

Before discussing the nature of dissipation, we first investigate the nature of this new SC system in terms of its dimensionality and the extent of the disorder. To study this, temperature dependent measurements of  $R_S(T)$  under perpendicular ( $B_\perp$ ) and parallel ( $B_\parallel$ ) magnetic fields have been carried out. Fig. 1d shows one representative set of data for current along  $[11\bar{2}]$  under low  $B_\perp$  (for other current orientation see Supplementary Fig. 3). Clearly, the SC is disrupted at very low magnetic field, which can be attributed to the low pinning of vortices in 2D superconductors.

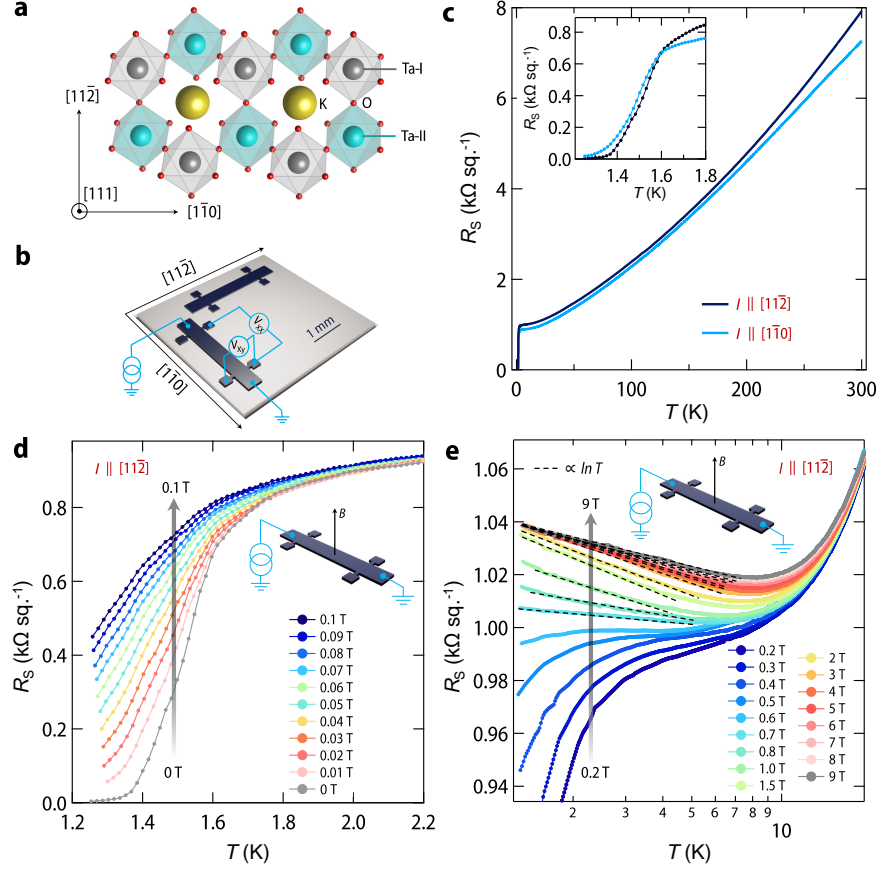


**FIG. 1. Device geometry and transport behavior of  $\text{AlO}_x/\text{KTaO}_3$  (111) interface** **a.** In a pure ionic picture, (111) oriented  $\text{KTaO}_3$  can be considered as a sequence of alternating  $[\text{KO}_3]^{5-}$  and  $\text{Ta}^{5+}$  planes. Arrangement of  $\text{Ta}^{5+}$  ions in two adjacent (111) planes are labelled by Ta-I and Ta-II [69]. **b.** Schematics of two Hall bars made on a  $\text{AlO}_x/\text{KTaO}_3$  (111) heterostructure. The width of the Hall bar is  $476\ \mu\text{m}$  and  $445\ \mu\text{m}$  for  $[11\bar{2}]$  and  $[1\bar{1}0]$  directions respectively and the length between the voltage probes is  $1.87\ \text{mm}$  for both the Hall bars. **c.** Temperature-dependent  $R_S$  for both the Hall bars for a  $7\ \text{nm}$   $\text{AlO}_x/\text{KTaO}_3$  (111) sample. Inset shows a magnified view around the superconducting transition temperature. The normal state  $R_S(T)$  shows a non Fermi liquid behavior ( $R_S \propto T^\alpha$  where  $\alpha < 2$ ) in a broad range of temperatures from  $75\ \text{K}$  to  $300\ \text{K}$  with  $\alpha = 1.5$  and  $1.3$  for current along  $[11\bar{2}]$  and  $[1\bar{1}0]$  respectively. This behavior is in sharp contrast with the  $T^3$  behavior observed in bulk electron doped  $\text{KTaO}_3$ , where no superconductivity has been observed (see Supplementary Fig 2). Low temperature variation of  $R_S$  under  $B_\perp$  has been shown in **d.** (from  $0\ \text{T}$  to  $0.1\ \text{T}$ ) and **e.** (from  $0.2\ \text{T}$  to  $9\ \text{T}$ ) for the Hall bar along  $[11\bar{2}]$ . Dotted lines in (**e**) show logarithmic dependence of  $R_S$  with the temperature near the avoided superconductor insulator transition.

Upon increasing the field, the sample avoids superconductor to insulator transition around  $R_S \sim 1 \text{ k}\Omega\text{sq.}^{-1}$  as seen in Fig. 1e. This result is in sharp contrast to the conventional theoretical framework that predicts a direct transition to an insulating state when the normal state sheet resistance approaches the quantum of resistance  $h/4e^2 = 6.45 \text{ k}\Omega \text{ sq.}^{-1}$  in the limit  $T \rightarrow 0$  [47, 48]. Such a behavior is generally observed in 2D superconductors with low disorder and has proven critically important for studying phases beyond the Landau Fermi liquid theory [49]. Interestingly, at higher  $B_\perp$  and lower  $T$ , our sample exhibits a logarithmic dependence of  $R_S$  on  $T$ . This logarithmic divergence is incompatible with the prediction of weak localization correction in 2D or Kondo effect [49] and is connected with the emergent granular nature of our conducting interface [50, 51].

To verify that superconductivity is 2D in nature, out of plane and in plane upper critical fields ( $B_{C\perp}$  and  $B_{C\parallel}$ ) have been measured. Fig. 2a shows the temperature dependence of  $B_{C\perp}$  obtained by tracking the evolution of superconducting transition,  $T_C$  with magnetic field from  $R_S$  vs.  $T$  plots. An appreciable difference in magnitude of  $B_{C\perp}$  is observed for two configurations of current. Higher value of  $B_{C\perp}$  for current along  $[11\bar{2}]$  direction is consistent with the observation of higher  $T_C$  for current along  $[11\bar{2}]$  direction. The solid line shows fitting with the Ginzburg-Landau (G-L) theory which predicts a linear  $T$  behavior of  $B_{C\perp}$  given by

$$B_{C\perp} = \frac{\Phi_0(1 - T/T_C)}{2\pi(\xi_0)^2} \quad (1)$$

where  $\Phi_0$  is the magnetic flux quantum and  $\xi_0$  is the G-L coherence length at  $T = 0 \text{ K}$ .  $\xi_0$  from fitting is found to be  $\sim 23.4 \text{ nm}$  and  $21.4 \text{ nm}$  for current along  $[11\bar{2}]$  and  $[1\bar{1}0]$  directions, respectively. Fig. 2b shows the temperature evolution of  $B_{C\parallel}$  for the case when current is parallel to the in plane magnetic field (see Supplementary Figs. 4, 5 and 6 for  $R_S$  vs.  $T$  plots and data for other configurations of current). Similar to the out of plane measurement, the magnitude of  $B_{C\parallel}$  is found to be larger for the current along  $[11\bar{2}]$  direction. The temperature dependence of  $B_{C\parallel}$  shows a characteristic square-root dependence (shown by the solid lines in Fig. 2b). Such a behavior is consistent with the Tinkham's model [52] where  $B_{C\parallel}$  is given by

$$B_{C\parallel} = \frac{\Phi_0[12(1 - T/T_C)]^{1/2}}{2\pi d\xi_0} \quad (2)$$

where  $d$  is the effective thickness of the superconducting region. The estimated thickness of superconducting region is found to be  $\sim 5 \text{ nm}$  which is much less than phase coherence length, signifying two dimensional nature of the superconductivity at the  $\text{AlO}_x/\text{KTO}$  (111) interface. Interestingly, the value of the in plane upper critical field extrapolated to  $0 \text{ K}$  is found to be much

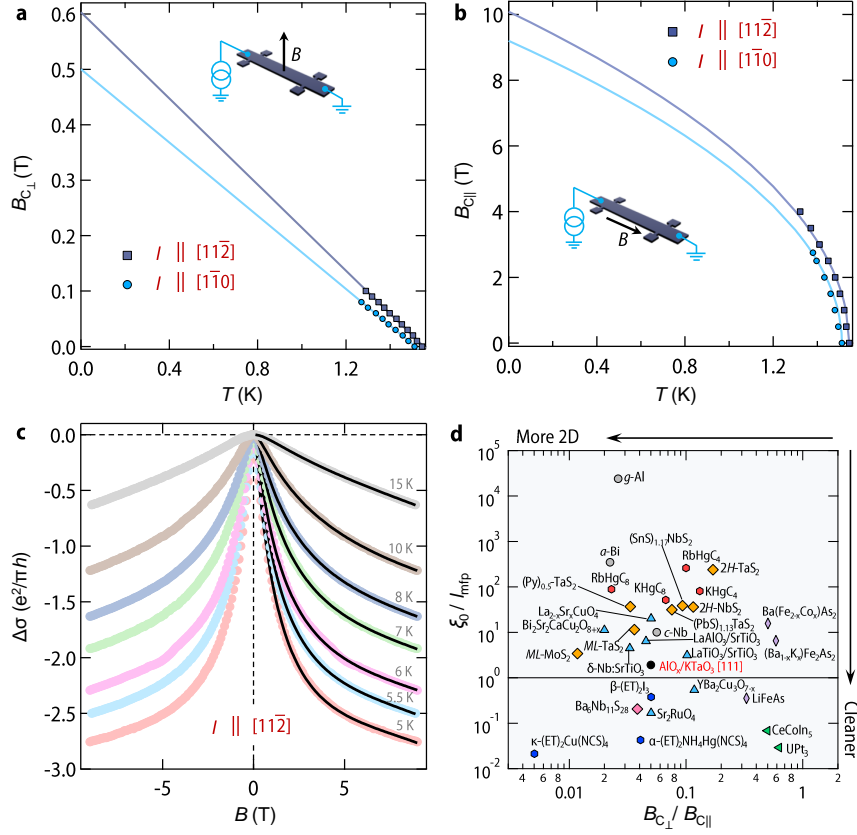


**FIG. 2. Critical field, weak anti-localization, and the extent of disorder** **a.** Temperature dependence of out of plane upper critical field ( $B_{C\perp}$ ) for  $I$  along  $[11\bar{2}]$  and  $[1\bar{1}0]$ . The solid line denotes fitting with Ginzburg-Landau theory. **b.** Temperature dependence of in-plane upper critical field ( $B_{C\parallel}$ ) for  $I$  along  $[11\bar{2}]$  and  $[1\bar{1}0]$ . Further,  $B$  is parallel to the current direction. The solid line denotes fitting with Tinkham's model. **c.** Sheet conductance difference ( $\Delta\sigma = \sigma(B) - \sigma(B=0)$ ,  $\sigma = 1/R_S(B)$ ) in the units of  $e^2/\pi h$  for the Hall bar with  $I$  along  $[11\bar{2}]$ . The black solid curves show the fitting with ILP (Iordanskii, Lyanda-Geller, and Pikus) theory [70, 71] (without considering linear Rashba term) including a classical  $B^2$  term (also see Supplementary Note 2 and Supplementary Fig. 7 for fitting details). **d.** Phase diagram of several superconducting compounds categorized by their extent of 2D character and cleanliness. 2D character is resembled by the anisotropy of critical field defined by  $(B_{C\perp}/B_{C\parallel})$  and extent of disorder is quantified by the ratio between phase coherence length and electronic mean free path ( $\xi_0/l_{mfp}$ ). Assuming a single isotropic band in 2D,  $l_{mfp}$  is given by  $l_{mfp} = h/(e^2 k_F R_S)$ , where  $k_F = (2\pi n_s)^{1/2}$  is the Fermi wave vector and  $n_s$  is the sheet carrier density. From the measured  $n_s$  (at 5 K) and  $R_S$  (at 5 K), the  $l_{mfp}$  is estimated to be  $\sim 12$  nm for the present case. The value of all the parameters for other compounds have been largely taken from the reference [56] except for the  $\text{LaTiO}_3/\text{SrTiO}_3$  interface which has been taken from [37]. As evident,  $\text{AlO}_x/\text{KTaO}_3(111)$  is located very near to the boundary between clean and dirty limits, denoted by a horizontal solid line.

larger ( $\sim 10$  T) than Clogston Chandrasekhar limit [53, 54]. Such a large value of  $B_{C\parallel}$  is generally expected in systems with a strong SOC [55] and the observation of weak antilocalization characteristics in longitudinal magnetoconductance data within the normal phase (see Fig. 2c) demonstrates the importance of SOC in the present case.

In order to examine the extent of disorder in our system, we have estimated the ratio of  $\xi_0$  and the electronic mean free path  $l_{\text{mfp}}$ . The ratio is close to 2, emphasizing that the SC at  $\text{AlO}_x/\text{KTO}$  (111) interface falls in the intermediate disorder regime (see Fig. 2d), making it an interesting system for simultaneous investigation of dissipation pertaining to an ideal BKT system and also arising from the inhomogeneous electronic structure using a single sample [56]. The presence of oxygen vacancies at the interface are one of the most prominent sources of disorder in the system. Clustering of oxygen vacancies can also lead to a very local inhomogeneous electronic structure in the real space [57]. Apart from such local inhomogeneities, there is another source of inhomogeneity, which happens at a much larger scale, known as electronic phase separation (EPS) [29–32]. EPS has been routinely observed in STO based 2DEGs and is very often associated with the presence of multi carriers at the interface. The observation of two types of electrons with densities  $n_1$  and  $n_2$  with mobility  $\mu_1$ , and  $\mu_2$ , respectively ( $n_1 \gg n_2$  and  $\mu_1 < \mu_2$ ) in our Hall effect measurements (see Supplementary Notes 3, 4 and 5 and accompanying Supplementary Figs. 8, 9 and 10) strongly suggests that a similar scenario can also be applicable in our samples. As a general consequence of EPS, superconducting puddles joined by weak links would emerge naturally in real space [38], making the SC strongly inhomogeneous. This mechanism is likely a dominant cause for the observed granular nature of our system. Note that EPS could also arise due to the Rashba SOC [29] which is also quite generic to our system.

**Various regions of dissipations as a function of  $dc$  current:** Having established the nature of inhomogeneities in our 2D superconducting system, we now explore the nature of dissipation under  $dc$  current bias. For this, comprehensive  $I$ - $V$  measurements have been performed. Fig. 3a shows the  $I$ - $V$  curves taken in forward and backward sweeps at several fixed temperatures from 1.26 K to 10 K for current along  $[11\bar{2}]$  direction under zero magnetic field. All data has been shifted vertically upwards for visual clarity. Broadly four distinct regimes can be identified in the  $I$ - $V$  curve at the lowest temperature (1.26 K) of our measurements: (1) At small currents (less than  $60 \mu\text{A}$ - $70 \mu\text{A}$ ) while voltage drop looks almost independent of  $I$ , a small voltage drop always appears (see Fig. 3b)) due to breaking of few weakly bound vortex-antivortex pairs as the critical current for breaking of vortex-antivortex is zero [12, 58]. (2) Above this regime, a non-linear



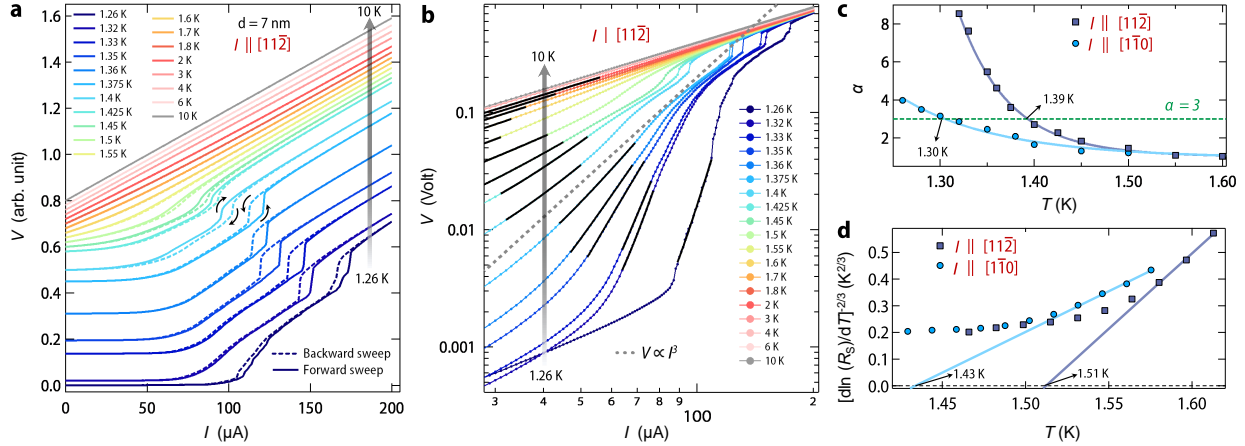


**FIG. 3. Current voltage ( $I$ - $V$ ) characteristics and determination of  $T_{\text{BKT}}$**  **a.** Temperature dependent  $I$ - $V$  curves measured in current bias mode for the Hall bar along  $[11\bar{2}]$ . Solid and dotted curves denote forward and backward sweeps, respectively. Curves have been shifted upward for visual clarity. **b.**  $I$ - $V$  curves in logarithmic scale during the forward sweep. The solid black line shows the fit with the power law given by  $V \propto I^\alpha$ . A dotted gray line corresponds to  $\alpha=3$  where the Berezinskii Kosterlitz Thouless transition takes place. **c.** Temperature dependence of  $\alpha$  for  $I$  along  $[11\bar{2}]$  and  $[1\bar{1}0]$ . A dotted green line shows a constant line for  $\alpha=3$ . From the crossover of  $\alpha$  around 3,  $T_{\text{BKT}}$  is found out to be 1.39 K and 1.30 K for the Hall bar along  $[11\bar{2}]$  and  $[1\bar{1}0]$ , respectively. **d.** The value of  $T_{\text{BKT}}$  is also estimated using the Halperin-Nelson model ( $R_S=R_0\exp[-b/(T-T_{\text{BKT}})^{1/2}]$  where  $b$  is the vortex-antivortex interaction strength) [63, 72]. To estimate  $T_{\text{BKT}}$  using this model,  $d\ln(R_S)/dT^{2/3}$  has been plotted as a function of  $T$ , near the superconducting transition temperature. By finding the  $x$  axis intercept of this plot, we find  $T_{\text{BKT}} \sim 1.51$  K and 1.43 K for the Hall bar along  $[11\bar{2}]$  and  $[1\bar{1}0]$ , respectively. These values are very close to the  $T_{\text{BKT}}$ , obtained in (c).

behavior appears in a very short window from  $\sim 80 \mu\text{A}$ - $110 \mu\text{A}$ . (3) This regime then translates into a region from  $110 \mu\text{A}$  to  $175 \mu\text{A}$ , where the majority of the dissipation happens as observed by a large change in the voltage drop. (4) Above  $175 \mu\text{A}$ , the magnitude of  $V$  grows almost in proportion to the applied current and finally enters into the regime of ohmic dissipation. All these different regions in  $I$ - $V$  characteristics are strongly  $T$  dependent. The first and fourth regimes are well understood [1, 12] and are skipped from further discussions.

We first discuss the origin of non-linear  $I$ - $V$ , observed just above the 1<sup>st</sup> regime. This regime corresponds to the intrinsic dissipation of a BKT system which is characterized by power law behavior ( $V \propto I^\alpha$ ) arising from current driven unbinding of thermally generated vortex-antivortex

pairs near the BKT transition [9, 10]. This behavior becomes much more evident in the logarithmic plot (Fig. 3b), where power law translates into a linear behavior. The value of  $\alpha$  becomes exactly 3 at the  $T_{\text{BKT}}$  (shown by a dotted gray line ( $V \propto I^3$ ) in Fig. 3b) and is routinely used to trace out BKT phase transition in 2D superconductors.  $T_{\text{BKT}}$  is estimated to be 1.39 K and 1.30 K (Fig. 3c) for the Hall bar along  $[11\bar{2}]$  and  $[1\bar{1}0]$ , respectively, from such analysis (also see Fig. 3d).

**Demonstration of LO-type FFI:** We next focus on the nature of dissipation beyond power-law regime. At the lowest temperature of our measurement 1.26 K, which is below  $T_{\text{BKT}}$ , dissipation happens via discrete jumps in the measured voltage, which is much more evident from the  $dV/dI$  plot shown in Supplementary Fig. 11. These are reminiscent of phase slip events generally observed in 1D superconducting wire [1]. On the contrary, formation of hot-spots [59] and flux-flow instability [18, 21] are the two widely accepted cause for such discrete jumps under large current in thin film geometry. Hot-spots are the regions in real space with temperature higher than the  $T_{\text{C}}$ , which appear due to the Joule self-heating in inhomogeneous systems [60]. In presence of hot-spots,  $I$ - $V$  curve takes the shape of ‘S’, which would lead to a hysteresis between forward and reverse current bias (see Fig. 4a). In the present case, hot-spots are most likely to occur near the weak links joining the superconducting puddles, appearing due to the granular nature of SC as discussed earlier.

Apart from the hot-spot effect, LO type FFI is another phenomena which leads to a ‘S’ shape  $I$ - $V$  characteristics with similar voltage instabilities in current bias mode due to ultra-fast vortices [18, 19]. While the original LO instability was predicted for type II superconductors under magnetic field, we demonstrate here that such unusual phenomenon can be observed in 2D superconductors, even in absence of a magnetic field. This is due to the fact that free vortices can be generated in 2D superconductors either by thermal fluctuation in the temperature range  $T_{\text{BKT}} \leq T \leq T_{\text{C}}$  [11, 61] or by breaking of thermally induced vortex-antivortex pairs by current below  $T_{\text{BKT}}$  [10]. In the following, we test the applicability and predictions of LO theory for the  $\text{AlO}_x/\text{KTO}$  (111) superconductor. We further emphasize that the magnetic field generated due to current flowing through the sample or residual field in the magnet is too small and has no role for our observation (see Supplementary Notes 6 and 7 and accompanying Supplementary Figs. 12 and 13).

1. The whole LO theory of FFI was built on the argument that at large vortex velocities, quasiparticles at the core of the vortex can reach energies above the superconducting energy gap ( $\Delta$ ) due to its acceleration under electric field created due to flux-flow and ultimately diffuse

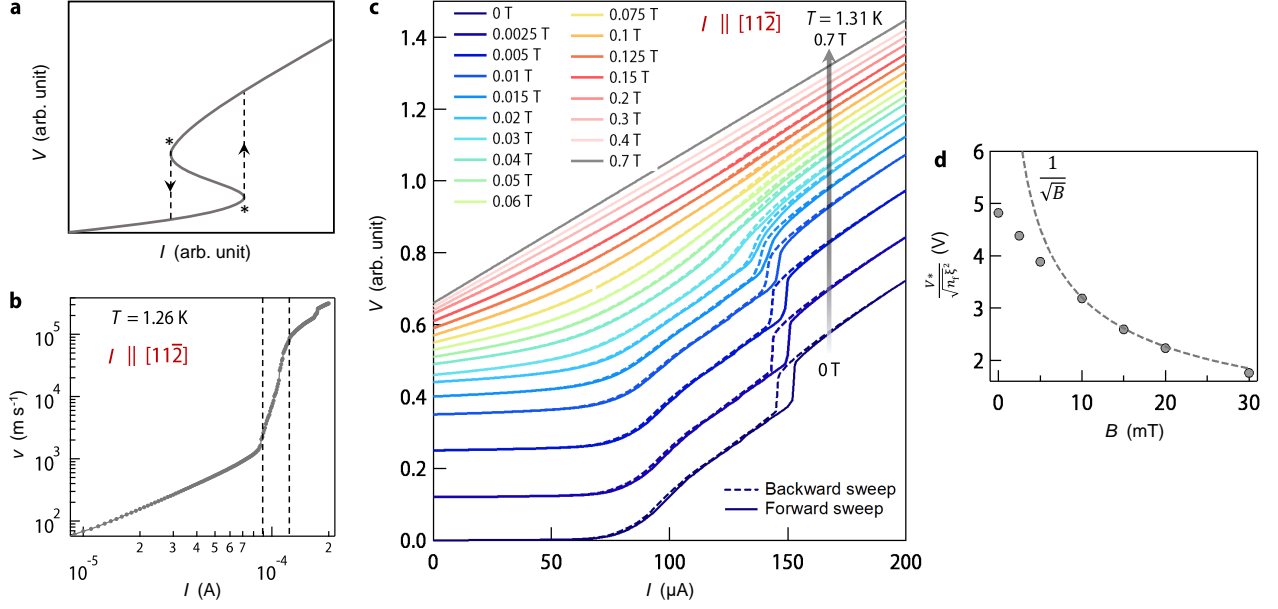


**FIG. 4. Evidence for flux-flow instability** **a.** A schematic depicting 'S' shaped  $I$ - $V$  characteristics, which has two unstable points, denoted by \* symbol. When the  $I$ - $V$  measurement is performed in current bias mode, a voltage instability is observed when the value of current is close to unstable point leading to an abrupt increase/decrease in the voltage drop. Further, the voltage instability under backward current sweep happens at a lower current than in the forward sweep leading to a hysteresis. **b.** Current dependent vortex velocity at 1.26 K for 7 nm  $\text{AlO}_x/\text{KTaO}_3$  (111) ( $I$  along  $[11\bar{2}]$ ). We emphasize that this whole analysis only holds only in between the region marked with the dashed lines [28]. **c.** Magnetic field dependent  $I$ - $V$  curves measured in current bias mode for the Hall bar along  $[11\bar{2}]$  on 7nm  $\text{AlO}_x/\text{KTaO}_3$  (111) sample at 1.31 K. Curves have been shifted upward for visual clarity. **d.** Magnetic field evolution of normalized critical voltage ( $\frac{V^*}{\sqrt{n_f \xi^2}}$ ) calculated for Hall bar along  $[11\bar{2}]$  on 7 nm  $\text{AlO}_x/\text{KTaO}_3$  (111) sample. The dotted line denotes expected behavior for  $\frac{1}{\sqrt{B}}$  dependence.

away from the core. During this process, the core of the vortex starts shrinking and resultantly, the viscous damping coefficient ( $\eta$ ) becomes a function of vortex velocity which is given by the formula [18, 19]

$$\eta(v) = \eta(0) \frac{1}{1 + (v/v^*)^2} \quad (3)$$

where  $v^*$  is the critical vortex velocity, where FFI would occur. As evident from the above equa-

tion,  $\eta$  decreases with increasing  $v$ , leading to an ever increasing vortex velocity and after the critical velocity  $v^*$ , the system becomes unstable, leading to a voltage jump in  $I$ - $V$  curve.

In order to check this, we have calculated the vortex velocity (see Supplementary Note 8) using the Gor'kov–Josephson relation [62, 63]. Fig. 4b shows the calculated velocity for 7 nm AlO<sub>x</sub>/KTO (111) sample at 1.26 K in zero magnetic field. As evident, there is almost two orders of magnitude abrupt increase in the vortex velocity (see Fig. 4b), consistent with the LO-type FFI. Moreover, the maximum velocity ( $\sim 10^5$  ms<sup>-1</sup>) is much higher than the Abrikosov vortex velocity ( $\sim 10^3$  ms<sup>-1</sup>) [1], and is also very similar to what has been reported earlier for other systems exhibiting LO-type instability under magnetic field [27].

2. In the original LO picture, the sample is assumed to be in perfect thermal equilibrium with the phonon bath and hence the effect of Joule heating on FFI is completely neglected. However, this may not be true in reality. In presence of overheating, a further modification has been suggested by Bezuglyj and Shklovskij [27, 64], which would lead to a  $B$  dependent  $v^*$  with functional form

$$v^* \propto z\Delta^{1/2}B^{-1/2} \quad (4)$$

where  $z$  is the heat removal coefficient. However, this relation was derived with the constraint that density of free vortices ( $n_f$ ) is independent of temperature, which is not the case in 2D superconductors. For BKT system, the expression for  $v^*$  in presence of overheating can be written as (see Supplementary Note 9)

$$v^* \propto \left( \frac{\Delta(T)\xi^2(T)}{n_f(T, B)} \right)^{1/2} B^{-1/2} \quad (5)$$

Since the exact temperature dependence of  $\xi$  is unknown, we rewrite the above equation using the Gor'kov–Josephson relation [62, 63] as

$$\frac{V^*}{\sqrt{n_f\xi^2}} \propto \Delta(T)^{1/2}B^{-1/2} \quad (6)$$

where  $V^*$  marks the onset of voltage instability in  $I$ - $V$  curve.

To testify this for present case, we have performed  $I$ - $V$  measurement in presence of  $B$  at a fixed temperature. Fig. 4c shows one representative set of data for Hall bar along  $[11\bar{2}]$  on 7nm AlO<sub>x</sub>/KTO (111) sample. As evident from Fig. 4d, normalized  $V^*$  is indeed dependent on  $B$  with a characteristic of  $B^{-1/2}$  dependence at higher fields (for calculation of the denominator in eq. 6, we refer to Supplementary Note 10). We note that, a similar behavior was observed for  $v^*$  in Nb-C

superconductor near  $T_C$  and the deviation from  $B^{-1/2}$  at low fields was attributed to the possible role of edge controlled FFI [27].

## DISCUSSIONS

Having demonstrated the relevance of hot-spots and LO type FFI in our samples, we next discuss the temperature evolution of these two effects. For this, we first note that since the specific heat transfer power from the sample to the thermal bath is not known at a given temperature, a quantitative estimation of relative contribution from the hot-spot and FFI can not be made. Nonetheless, our temperature dependent analysis of  $\frac{V^*}{\sqrt{n_f \xi^2}}$  indicates that the hot-spots are most likely effective below  $T_{\text{BKT}}$  whereas FFI would be more applicable close to  $T_C$  (see Supplementary Note 11 and Supplementary Fig. 14 ).

We next focus on the temperature evolution of the  $I$ - $V$  hysteresis [Fig. 3a] in our samples. The hysteresis is anticlockwise at the lowest temperature of our measurement, which can be attributed jointly to the formation of hot-spots and FFI as discussed earlier. Surprisingly, the nature of hysteresis changes completely from anticlockwise to clockwise above a certain temperature (highlighted by arrows in Fig. 3a). We have also observed the same behavior for another sample with 14 nm  $\text{AlO}_x$  thickness (see Supplementary Figs. 16, 17 and 18 for additional data on this sample). Such clockwise hysteresis is extremely rare [21] and has never been observed in any interfacial superconductors to the best of our knowledge. To visualize this drastic change in  $I$ - $V$  hysteresis, we further plot the maximum width of hysteresis ( $\delta I_c$ ) as a function of temperature. Fig. 5a corresponds to  $\delta I_c$  for Hall bar along  $[11\bar{2}]$  and  $[1\bar{1}0]$  directions (also see Supplementary Fig. 15) on 7 nm  $\text{AlO}_x/\text{KTO}$  (111) sample. Fig. 5b contains a similar set of data for the 14 nm  $\text{AlO}_x/\text{KTO}$  (111) sample. As clearly evident, hysteresis always changes its sign around the  $T_{\text{BKT}}$  and vanishes around  $T_C$  in all the four Hall bars, that we have investigated in this work. While the vanishing of anticlockwise hysteresis across  $T_{\text{BKT}}$  can be accounted by the disappearance of quasi 1D dissipating channels such as weak links [65], the clockwise hysteresis can not be explained by the hot-spot effect. Rather, the observation of clockwise hysteresis in  $I$ - $V$  can be explained by (i) vortex de-pinning like instabilities [66] or (ii) LO type FFI [21]. Since our sample is already in flux-flow regime (see Supplementary Note 12 and Supplementary Fig. 19) at currents much smaller than the current at which the voltage instability is observed, the possibility of vortex de-pinning like instabilities can be discarded [24]. We further recall the following proposition of

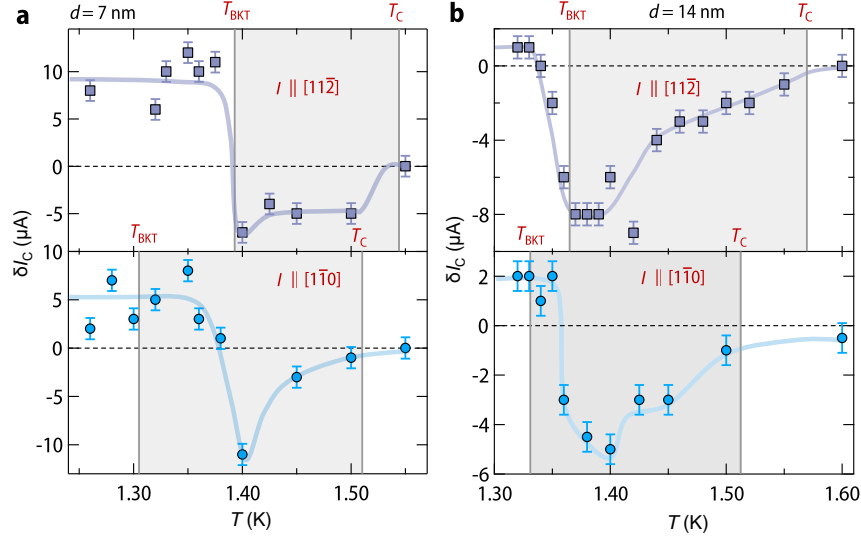


**FIG. 5. Sign change of hysteresis across Berezinskii Kosterlitz Thouless transition** **a.** Maximum width of hysteresis [ $\delta I_c = (I_c)_{\text{forward}} - (I_c)_{\text{backward}}$ ,  $(I_c)_{\text{forward}}$  and  $(I_c)_{\text{backward}}$  are the values of critical current in the middle of hysteresis in the forward and backward sweep, respectively] for  $I$  along  $[11\bar{2}]$  and  $[1\bar{1}0]$  for 7 nm  $\text{AlO}_x/\text{KTaO}_3$  (111) sample. **b.** Similar data for another sample with double the thickness (14 nm) of  $\text{AlO}_x$ . The sheet carrier density for this sample was found to be  $1.1 \times 10^{14} \text{cm}^{-2}$  at 300 K and the  $T_C$  is 1.57 K and 1.51 K for  $I$  along  $[11\bar{2}]$  and  $[1\bar{1}0]$  respectively, these values are very similar to the case of 7 nm  $\text{AlO}_x/\text{KTaO}_3$  (111) sample. The change in the width of the hysteresis upon multiple cycling has been used to estimate the error bar.

Samoilov et al. in the context of LO theory [21]. It was proposed that, once the superconductor is driven into the normal resistive state in the forward current sweep, the electron-electron (inelastic) scattering rate becomes higher (smaller  $\tau_e$ ) [21], leading to an electronic instability. This would mean that during the backward current sweep, the value of  $V^*$  will be higher ( $V^* \sim \tau_e^{-1/2}$ ) than that of the forward sweep (see Supplementary Note 9). This would automatically move the  $I$ - $V$  curve towards the higher current and would result to a clockwise hysteresis, as observed here. Moreover, the vanishing of clockwise hysteresis at  $T_C$  is consistent with the fact that vortices do not exist above  $T_C$ .

## CONCLUSIONS

In summary, our extensive analysis of temperature and magnetic field dependent  $I$ - $V$  measurement strongly emphasizes on the definite role of heating effects and FFI in determining the nature of dissipation at large current bias in inhomogeneous BKT systems. The in-plane anisotropy observed in the onset temperature of clockwise hysteresis between the two Hall bars with  $I$  along  $[1\bar{1}0]$  and  $[11\bar{2}]$  may arise from the in-plane anisotropy of critical vortex velocity for the onset of electronic instability. Such an observation is beyond the LO theory and calls for further investigations. Since the vortex structure in BKT system is strongly influenced by the presence of strong SOC [67], an extension of LO theory in presence of SOC and finite heating effects will be essential to understand such non-trivial feature. Future studies will focus on measurements beyond the intermediate disorder regime under simultaneous top and bottom gate, which will provide an independent investigation of the role of disorder and carrier density in determining the nature of dissipation under large current drive. Several recent studies, including those focused on magic angle twisted bilayer graphene [68], MoS<sub>2</sub> [28], and NbSe<sub>2</sub> [16], have observed anomalies in high-current  $I$ - $V$  characteristics, which have been explained qualitatively in terms of vortex instability/phase-slip lines. Our findings of FFI across the BKT phase transition could serve as a framework for comprehending dissipation in such diverse class of 2D superconductors subjected to large currents. Further exploration of this highly non-equilibrium phenomenon in other systems that exhibit BKT transition, such as trapped atomic gases and neutral superfluids, would be of significant interest.

## METHODS

**Sample growth and characterization:** AlO<sub>x</sub>/KTaO<sub>3</sub> (111) samples were fabricated by ablating a single crystalline Al<sub>2</sub>O<sub>3</sub> target on (111) oriented KTO substrate using a pulsed laser deposition system (Neocera LLC, USA) equipped with a high pressure reflection high energy electron diffraction setup (Staib instruments, Germany). A KrF excimer laser (Coherent, Germany) operated at a repetition rate of 1 Hz ( $\lambda=248$  nm) and an energy density  $\sim 1$  Jcm<sup>-2</sup> (on the target) was used for ablating the target. Target to substrate distance was fixed at 5.6 cm. The substrate was heated using a resistive heater whose temperature was maintained at 560 °C during the growth. The growth chamber pressure was  $5 \times 10^{-6}$  Torr during the deposition. Immediately after the ablation, the

sample was cooled to room temperature at a rate of  $15^{\circ}\text{Cmin}^{-1}$  under the vacuum. The surface morphology of the as received substrate and the film was monitored by performing atomic force microscopy (AFM) in non-contact mode using a Park AFM system. The thickness of the films was determined from X-ray reflectivity measurement performed in a lab based Rigaku Smartlab diffractometer. For more details, see Supplementary Note 1.

**Transport Measurements:** All the transport measurements were performed in an Oxford Integra LLD system using the standard four probe method in the Hall bar geometry. Ohmic contacts were made by ultrasonically bonding Al wire. Electrical resistance was measured using a *dc* delta mode with a Keithley 6221 current source and a Keithley 2182A nanovoltmeter and also using standard low-frequency lock-in technique. For *I-V* measurements, a Keithley 2450 source meter was used in current bias mode with a sweep rate of  $10\ \mu\text{As}^{-1}$ .

## DATA AVAILABILITY

The data that support the findings of this work are available from the corresponding authors upon reasonable request.

---

## REFERENCES

- [1] Tinkham, M. *Introduction to superconductivity* (Courier Corporation, 2004).
- [2] Bardeen, J. Critical fields and currents in superconductors. *Rev. Mod. Phys.* **34**, 667–681 (1962). URL <https://link.aps.org/doi/10.1103/RevModPhys.34.667>.
- [3] Embon, L. *et al.* Imaging of super-fast dynamics and flow instabilities of superconducting vortices. *Nature Communications* **8**, 85 (2017). URL <https://doi.org/10.1038/s41467-017-00089-3>.
- [4] Devoret, M. H. & Schoelkopf, R. J. Superconducting circuits for quantum information: An outlook. *Science* **339**, 1169–1174 (2013). URL <https://www.science.org/doi/abs/10.1126/science.1231930>. <https://www.science.org/doi/pdf/10.1126/science.1231930>.
- [5] Gurevich, A. & Ciovati, G. Dynamics of vortex penetration, jumpwise instabilities, and nonlinear surface resistance of type-ii superconductors in strong rf fields. *Phys. Rev. B* **77**, 104501 (2008). URL



- <https://link.aps.org/doi/10.1103/PhysRevB.77.104501>.
- [6] Welp, U., Kadowaki, K. & Kleiner, R. Superconducting emitters of thz radiation. *Nature Photonics* **7**, 702–710 (2013). URL <https://doi.org/10.1038/nphoton.2013.216>.
- [7] Berezinskii, V. Destruction of long-range order in one-dimensional and two-dimensional systems having a continuous symmetry group i. classical systems. *Sov. Phys. JETP* **32**, 493–500 (1971).
- [8] Kosterlitz, J. M. & Thouless, D. J. Ordering, metastability and phase transitions in two-dimensional systems. *Journal of Physics C: Solid State Physics* **6**, 1181–1203 (1973). URL <https://doi.org/10.1088/0022-3719/6/7/010>.
- [9] Beasley, M. R., Mooij, J. E. & Orlando, T. P. Possibility of vortex-antivortex pair dissociation in two-dimensional superconductors. *Phys. Rev. Lett.* **42**, 1165–1168 (1979). URL <https://link.aps.org/doi/10.1103/PhysRevLett.42.1165>.
- [10] Epstein, K., Goldman, A. M. & Kadin, A. M. Vortex-antivortex pair dissociation in two-dimensional superconductors. *Phys. Rev. Lett.* **47**, 534–537 (1981). URL <https://link.aps.org/doi/10.1103/PhysRevLett.47.534>.
- [11] Resnick, D. J., Garland, J. C., Boyd, J. T., Shoemaker, S. & Newrock, R. S. Kosterlitz-thouless transition in proximity-coupled superconducting arrays. *Phys. Rev. Lett.* **47**, 1542–1545 (1981). URL <https://link.aps.org/doi/10.1103/PhysRevLett.47.1542>.
- [12] Jos, J. V. *40 Years of Berezinskii-Kosterlitz-Thouless Theory* (World Scientific, 2013).
- [13] Andronov, A., Gordion, I., Kurin, V., Nefedov, I. & Shereshevsky, I. Kinematic vortices and phase slip lines in the dynamics of the resistive state of narrow superconductive thin film channels. *Physica C: Superconductivity and its Applications* **213**, 193–199 (1993). URL <https://www.sciencedirect.com/science/article/pii/092145349390777N>.
- [14] Weber, A. & Kramer, L. Dissipative states in a current-carrying superconducting film. *Journal of Low Temperature Physics* **84**, 289–299 (1991). URL <https://doi.org/10.1007/BF00683522>.
- [15] Sivakov, A. G. *et al.* Josephson behavior of phase-slip lines in wide superconducting strips. *Phys. Rev. Lett.* **91**, 267001 (2003). URL <https://link.aps.org/doi/10.1103/PhysRevLett.91.267001>.
- [16] Paradiso, N., Nguyen, A.-T., Enzo Kloss, K. & Strunk, C. Phase slip lines in superconducting few-layer NbSe<sub>2</sub> crystals. *2D Materials* **6**, 025039 (2019). URL <https://dx.doi.org/10.1088/2053-1583/ab0bcc>.

- [17] Berdiyrov, G. R., Milošević, M. V. & Peeters, F. M. Kinematic vortex-antivortex lines in strongly driven superconducting stripes. *Phys. Rev. B* **79**, 184506 (2009). URL <https://link.aps.org/doi/10.1103/PhysRevB.79.184506>.
- [18] Larkin, A. & Ovchinnikov, Y. Nonlinear conductivity of superconductors in the mixed state. *Sov. Phys. JETP* **41**, 960–965 (1975).
- [19] Klein, W., Huebener, R. P., Gauss, S. & Parisi, J. Nonlinearity in the flux-flow behavior of thin-film superconductors. *Journal of Low Temperature Physics* **61**, 413–432 (1985). URL <https://doi.org/10.1007/BF00683694>.
- [20] Doettinger, S. G. *et al.* Electronic instability at high flux-flow velocities in high- $T_c$  superconducting films. *Phys. Rev. Lett.* **73**, 1691–1694 (1994). URL <https://link.aps.org/doi/10.1103/PhysRevLett.73.1691>.
- [21] Samoilov, A., Konczykowski, M., Yeh, N.-C., Berry, S. & Tsuei, C. Electric-field-induced electronic instability in amorphous  $\text{Mo}_3\text{Si}$  superconducting films. *Physical review letters* **75**, 4118 (1995).
- [22] Ruck, B. J., Abele, J. C., Trodahl, H. J., Brown, S. A. & Lynam, P. Vortex dynamics and instabilities in layered and homogeneous Ta/Ge superconductors. *Phys. Rev. Lett.* **78**, 3378–3381 (1997). URL <https://link.aps.org/doi/10.1103/PhysRevLett.78.3378>.
- [23] Xiao, Z. L., Andrei, E. Y. & Ziemann, P. Coexistence of the hot-spot effect and flux-flow instability in high- $T_c$  superconducting films. *Phys. Rev. B* **58**, 11185–11188 (1998). URL <https://link.aps.org/doi/10.1103/PhysRevB.58.11185>.
- [24] Xiao, Z. L., Voss-de Haan, P., Jakob, G. & Adrian, H. Voltage jumps in current-voltage characteristics of  $\text{Bi}_2\text{Sr}_2\text{CaCu}_2\text{O}_{8+\delta}$  superconducting films: Evidence for flux-flow instability under the influence of self-heating. *Phys. Rev. B* **57**, R736–R739 (1998). URL <https://link.aps.org/doi/10.1103/PhysRevB.57.R736>.
- [25] Kunchur, M. N. Unstable flux flow due to heated electrons in superconducting films. *Phys. Rev. Lett.* **89**, 137005 (2002). URL <https://link.aps.org/doi/10.1103/PhysRevLett.89.137005>.
- [26] Babić, D., Bentner, J., Sürgers, C. & Strunk, C. Flux-flow instabilities in amorphous  $\text{Nb}_{0.7}\text{Ge}_{0.3}$  microbridges. *Phys. Rev. B* **69**, 092510 (2004). URL <https://link.aps.org/doi/10.1103/PhysRevB.69.092510>.
- [27] Dobrovolskiy, O. V. *et al.* Ultra-fast vortex motion in a direct-write nb-c superconductor. *Nature Communications* **11**, 3291 (2020). URL <https://doi.org/10.1038/s41467-020-16987-y>.

- [28] Saito, Y., Itahashi, Y. M., Nojima, T. & Iwasa, Y. Dynamical vortex phase diagram of two-dimensional superconductivity in gated MoS<sub>2</sub>. *Phys. Rev. Materials* **4**, 074003 (2020). URL <https://link.aps.org/doi/10.1103/PhysRevMaterials.4.074003>.
- [29] Caprara, S., Peronaci, F. & Grilli, M. Intrinsic instability of electronic interfaces with strong rashba coupling. *Phys. Rev. Lett.* **109**, 196401 (2012). URL <https://link.aps.org/doi/10.1103/PhysRevLett.109.196401>.
- [30] Caprara, S. *et al.* Inhomogeneous multi carrier superconductivity at LaXO<sub>3</sub>/SrTiO<sub>3</sub> (x = Al or Ti) oxide interfaces. *Superconductor Science and Technology* **28**, 014002 (2014). URL <https://doi.org/10.1088/0953-2048/28/1/014002>.
- [31] Caprara, S. *et al.* Multiband superconductivity and nanoscale inhomogeneity at oxide interfaces. *Phys. Rev. B* **88**, 020504 (2013). URL <https://link.aps.org/doi/10.1103/PhysRevB.88.020504>.
- [32] Ariando *et al.* Electronic phase separation at the LaAlO<sub>3</sub>/SrTiO<sub>3</sub> interface. *Nature Communications* **2**, 188 (2011). URL <https://doi.org/10.1038/ncomms1192>.
- [33] Likharev, K. K. Superconducting weak links. *Rev. Mod. Phys.* **51**, 101–159 (1979). URL <https://link.aps.org/doi/10.1103/RevModPhys.51.101>.
- [34] Benyamini, A. *et al.* Fragility of the dissipationless state in clean two-dimensional superconductors. *Nature Physics* **15**, 947–953 (2019). URL <https://doi.org/10.1038/s41567-019-0571-z>.
- [35] Reyren, N. *et al.* Superconducting interfaces between insulating oxides. *Science* **317**, 1196–1199 (2007).
- [36] Kozuka, Y. *et al.* Two-dimensional normal-state quantum oscillations in a superconducting heterostructure. *Nature* **462**, 487–490 (2009). URL <https://doi.org/10.1038/nature08566>.
- [37] Biscaras, J. *et al.* Two-dimensional superconductivity at a mott insulator/band insulator interface latio<sub>3</sub>/srtio<sub>3</sub>. *Nature Communications* **1**, 89 (2010). URL <https://doi.org/10.1038/ncomms1084>.
- [38] Chen, Z. *et al.* Carrier density and disorder tuned superconductor-metal transition in a two-dimensional electron system. *Nature Communications* **9**, 4008 (2018). URL <https://doi.org/10.1038/s41467-018-06444-2>.
- [39] Changjiang, L. *et al.* Two-dimensional superconductivity and anisotropic transport at KTaO<sub>3</sub> (111) interfaces. *Science* **371**, 716–721 (2021). URL <https://doi.org/10.1126/science>.

aba5511.

- [40] Zheng, C. *et al.* Electric field control of superconductivity at the LaAlO<sub>3</sub>/KTaO<sub>3</sub> (111) interface. *Science* **372**, 721–724 (2021). URL <https://doi.org/10.1126/science.abb3848>.
- [41] Ren, T. *et al.* Two-dimensional superconductivity at the surfaces of KTaO<sub>3</sub> gated with ionic liquid. *Science Advances* **8**, eabn4273 (2022). URL <https://www.science.org/doi/abs/10.1126/sciadv.abn4273>. <https://www.science.org/doi/pdf/10.1126/sciadv.abn4273>.
- [42] Mallik, S. *et al.* Superfluid stiffness of a ktao3-based two-dimensional electron gas. *Nature Communications* **13**, 4625 (2022). URL <https://doi.org/10.1038/s41467-022-32242-y>.
- [43] Pai, Y.-Y., Tylan-Tyler, A., Irvin, P. & Levy, J. Physics of SrTiO<sub>3</sub>-based heterostructures and nanostructures: a review. *Reports on Progress in Physics* **81**, 036503 (2018). URL <https://dx.doi.org/10.1088/1361-6633/aa892d>.
- [44] Liu, C. *et al.* Tunable superconductivity and its origin at KTaO<sub>3</sub> interfaces. *Nature Communications* **14**, 951 (2023). URL <https://doi.org/10.1038/s41467-023-36309-2>.
- [45] Cui-Zu, C. *et al.* Experimental observation of the quantum anomalous hall effect in a magnetic topological insulator. *Science* **340**, 167–170 (2013). URL <https://doi.org/10.1126/science.1234414>.
- [46] Ojha, S. K. *et al.* Electron trapping and detrapping in an oxide two-dimensional electron gas: The role of ferroelastic twin walls. *Phys. Rev. Applied* **15**, 054008 (2021). URL <https://link.aps.org/doi/10.1103/PhysRevApplied.15.054008>.
- [47] Goldman, A. M. & Marković, N. Superconductor-insulator transitions in the two-dimensional limit. *Physics Today* **51**, 39–44 (1998). URL <https://doi.org/10.1063/1.882069>.
- [48] Haviland, D. B., Liu, Y. & Goldman, A. M. Onset of superconductivity in the two-dimensional limit. *Phys. Rev. Lett.* **62**, 2180–2183 (1989). URL <https://link.aps.org/doi/10.1103/PhysRevLett.62.2180>.
- [49] Kapitulnik, A., Kivelson, S. A. & Spivak, B. Colloquium: Anomalous metals: Failed superconductors. *Rev. Mod. Phys.* **91**, 011002 (2019). URL <https://link.aps.org/doi/10.1103/RevModPhys.91.011002>.
- [50] Beloborodov, I. S., Lopatin, A. V., Vinokur, V. M. & Efetov, K. B. Granular electronic systems. *Rev. Mod. Phys.* **79**, 469–518 (2007). URL <https://link.aps.org/doi/10.1103/RevModPhys.79.469>.

- [51] Zhang, X., Hen, B., Palevski, A. & Kapitulnik, A. Robust anomalous metallic states and vestiges of self-duality in two-dimensional granular in-inox composites. *npj Quantum Materials* **6**, 30 (2021). URL <https://doi.org/10.1038/s41535-021-00329-2>.
- [52] Tinkham, M. Effect of fluxoid quantization on transitions of superconducting films. *Phys. Rev.* **129**, 2413–2422 (1963). URL <https://link.aps.org/doi/10.1103/PhysRev.129.2413>.
- [53] Chandrasekhar, B. S. A note on the maximum critical field of high-field superconductors. *Applied Physics Letters* **1**, 7–8 (1962). URL <https://doi.org/10.1063/1.1777362>.
- [54] Clogston, A. M. Upper limit for the critical field in hard superconductors. *Phys. Rev. Lett.* **9**, 266–267 (1962). URL <https://link.aps.org/doi/10.1103/PhysRevLett.9.266>.
- [55] Werthamer, N. R., Helfand, E. & Hohenberg, P. C. Temperature and purity dependence of the superconducting critical field,  $H_{c2}$ . iii. electron spin and spin-orbit effects. *Phys. Rev.* **147**, 295–302 (1966). URL <https://link.aps.org/doi/10.1103/PhysRev.147.295>.
- [56] A., D. *et al.* Clean 2d superconductivity in a bulk van der waals superlattice. *Science* **370**, 231–236 (2020). URL <https://doi.org/10.1126/science.aaz6643>.
- [57] Ojha, S. K. *et al.* Oxygen vacancy induced electronic structure modification of  $\text{KTaO}_3$ . *Phys. Rev. B* **103**, 085120 (2021). URL <https://link.aps.org/doi/10.1103/PhysRevB.103.085120>.
- [58] Kadin, A. M., Epstein, K. & Goldman, A. M. Renormalization and the kosterlitz-thouless transition in a two-dimensional superconductor. *Phys. Rev. B* **27**, 6691–6702 (1983). URL <https://link.aps.org/doi/10.1103/PhysRevB.27.6691>.
- [59] Gurevich, A. V. & Mints, R. G. Self-heating in normal metals and superconductors. *Rev. Mod. Phys.* **59**, 941–999 (1987). URL <https://link.aps.org/doi/10.1103/RevModPhys.59.941>.
- [60] Skocpol, W. J., Beasley, M. R. & Tinkham, M. Self-heating hotspots in superconducting thin-film microbridges. *Journal of Applied Physics* **45**, 4054–4066 (1974). URL <https://doi.org/10.1063/1.1663912>.
- [61] Doniach, S. & Huberman, B. A. Topological excitations in two-dimensional superconductors. *Phys. Rev. Lett.* **42**, 1169–1172 (1979). URL <https://link.aps.org/doi/10.1103/PhysRevLett.42.1169>.
- [62] Josephson, B. D. Supercurrents through barriers. *Advances in Physics* **14**, 419–451 (1965). URL <https://doi.org/10.1080/00018736500101091>.

- [63] Halperin, B. I. & Nelson, D. R. Resistive transition in superconducting films. *Journal of Low Temperature Physics* **36**, 599–616 (1979). URL <https://doi.org/10.1007/BF00116988>.
- [64] Bezuglyj, A. I. & Shklovskij, V. A. Effect of self-heating on flux flow instability in a superconductor near  $t_c$ . *Physica C: Superconductivity* **202**, 234–242 (1992). URL <https://www.sciencedirect.com/science/article/pii/0921453492901659>.
- [65] Ovadyahu, Z. Transition to zero vorticity in a two-dimensional superconductor. *Phys. Rev. Lett.* **45**, 375–378 (1980). URL <https://link.aps.org/doi/10.1103/PhysRevLett.45.375>.
- [66] Liu, Y. *et al.* Hysteresis effect in inhomogeneous superconductors. *Phys. Rev. B* **66**, 144510 (2002). URL <https://link.aps.org/doi/10.1103/PhysRevB.66.144510>.
- [67] Devreese, J. P. A., Tempere, J. & Sá de Melo, C. A. R. Effects of spin-orbit coupling on the berezinskii-kosterlitz-thouless transition and the vortex-antivortex structure in two-dimensional fermi gases. *Phys. Rev. Lett.* **113**, 165304 (2014). URL <https://link.aps.org/doi/10.1103/PhysRevLett.113.165304>.
- [68] Cao, Y., Park, J. M., Watanabe, K., Taniguchi, T. & Jarillo-Herrero, P. Pauli-limit violation and re-entrant superconductivity in moiré graphene. *Nature* **595**, 526–531 (2021). URL <https://doi.org/10.1038/s41586-021-03685-y>.
- [69] Xiao, D., Zhu, W., Ran, Y., Nagaosa, N. & Okamoto, S. Interface engineering of quantum hall effects in digital transition metal oxide heterostructures. *Nature Communications* **2**, 596 (2011). URL <https://doi.org/10.1038/ncomms1602>.
- [70] Iordanskii, S., Lyanda-Geller, Y. B. & Pikus, G. Weak localization in quantum wells with spin-orbit interaction. *ZhETF Pisma Redaktsiiu* **60**, 199 (1994).
- [71] Ojha, S. K. *et al.* Oxygen vacancy-induced topological hall effect in a nonmagnetic band insulator. *Advanced Quantum Technologies* **3**, 2000021 (2020). URL <https://doi.org/10.1002/qute.202000021>.
- [72] Minnhagen, P. The two-dimensional coulomb gas, vortex unbinding, and superfluid-superconducting films. *Rev. Mod. Phys.* **59**, 1001–1066 (1987). URL <https://link.aps.org/doi/10.1103/RevModPhys.59.1001>.

## **ACKNOWLEDGEMENTS**

Authors are thankful to Prof. Jak Chakhalian, Prof. Sumilan Banerjee, Prof. Manish Jain, Prof. Vibhor Singh and Sanat Kumar Gogoi for fruitful discussions and valuable comments about the manuscript. SM acknowledges a Department of Science and Technology (DST) Nanomission grant (DST/NM/NS/2018/246), SERB, India (Early Career Research Award: ECR/2018/001512, I.R.H.P.A Grant No. IPA/2020/000034), MHRD, Government of India under STARS research funding (STARS/APR2019/PS/156/FS) for financial support. The authors acknowledge the AFM, XRD, and wire bonding facility at the Department of Physics, IISc Bangalore. We are also thankful to Ranjan Kumar Patel for proofreading.

## **AUTHOR CONTRIBUTION**

SM conceived and supervised the experiments. SKO, PM carried out all experiments and contributed to data analysis and interpretation. SK, JM contributed in the initial experiments. SKO, PM, and SM wrote the paper. All authors discussed the results.

## **COMPETING INTERESTS**

The authors declare no competing interests.

## **ADDITIONAL INFORMATION**

The online version contains supplementary information.

# Supplementary Information

## Supplementary Note 1: Growth and characterization of $\text{AlO}_x/\text{KTaO}_3$ (111) sample

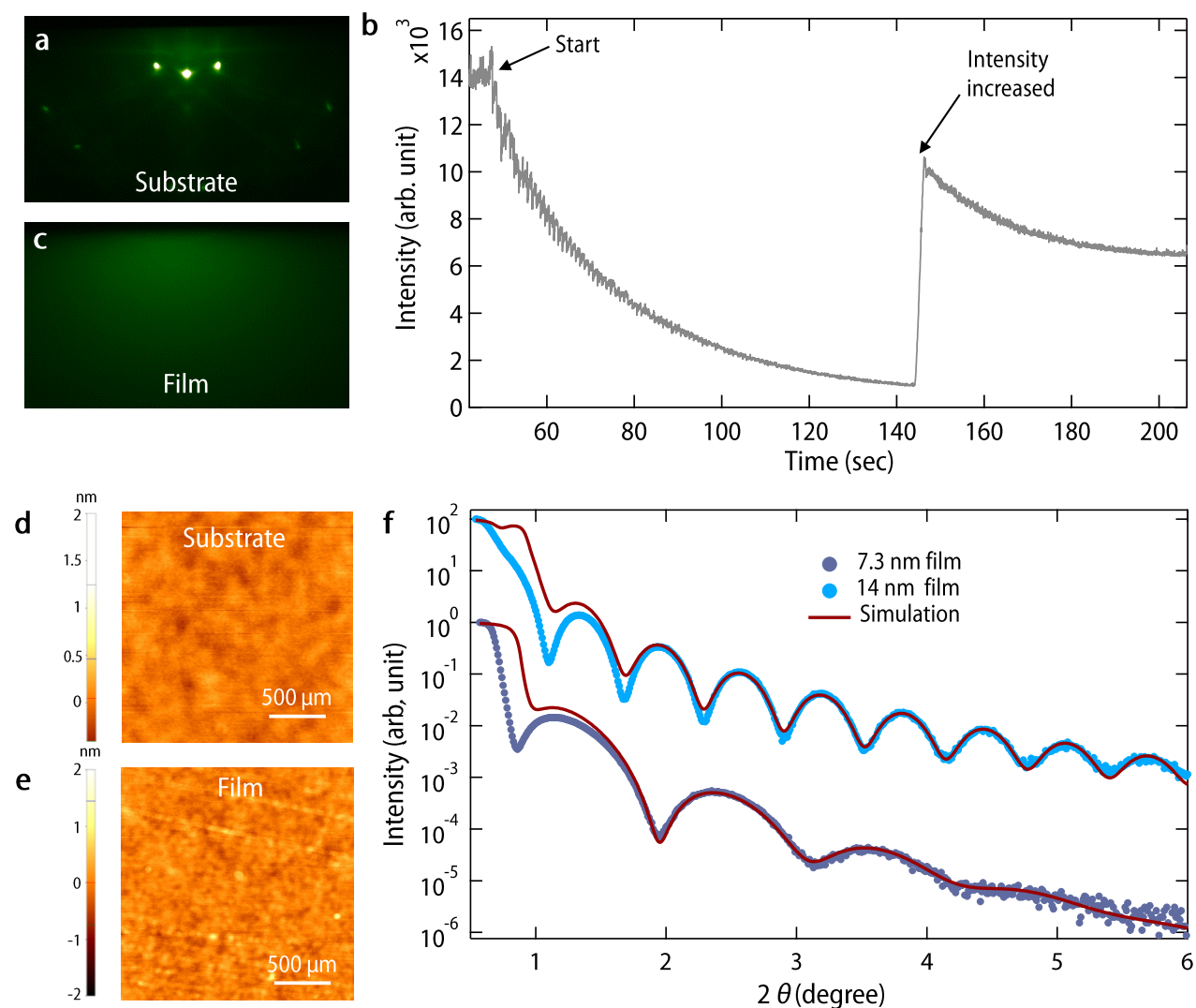


FIG. S1. **a.** Reflection high energy electron diffraction image of  $\text{KTaO}_3$  (111) substrate. The intensity of the specular spot during the growth of the film and just after the deposition of the film has been shown in the panels **b.** and **c.** respectively. Atomic force microscope image of the substrate and the film has been shown in panels **d.** and **e.** respectively. **f.** X-ray reflectivity pattern of the heterostructure along with the simulation.

Supplementary Figure S1a shows the reflection high energy electron diffraction (RHEED) image of as received  $\text{KTaO}_3$  (111) substrate. Observation of intense diffraction spots along with



Kikuchi lines establishes the flat and single crystalline nature of the surface and further excludes the possibility of faceting [1, 2]. This is further evident from the atomic force microscopy image of the substrate, which exhibits a very smooth surface morphology with mean roughness ( $R_q$ ) $\sim$  100 pm (Supplementary Figure S1d). Supplementary Figure S1b shows the temporal evolution of the intensity of the specular RHEED spot during the film deposition. As evident, intensity decreases gradually during the growth. This is due to the amorphous nature of the film which is evident from the absence of any diffraction spots in the RHEED image after the deposition (Supplementary Figure S1c). The resultant film has very flat surface morphology (Supplementary Figure S1e) with  $R_q$  $\sim$  175 pm. In order to determine the thickness of the films, X-ray reflectivity measurements have been performed. Supplementary Figure S1f shows the measured data along with the simulation (using GenX [3]) for two representative samples with thicknesses  $\sim$ 7 nm and 14 nm.

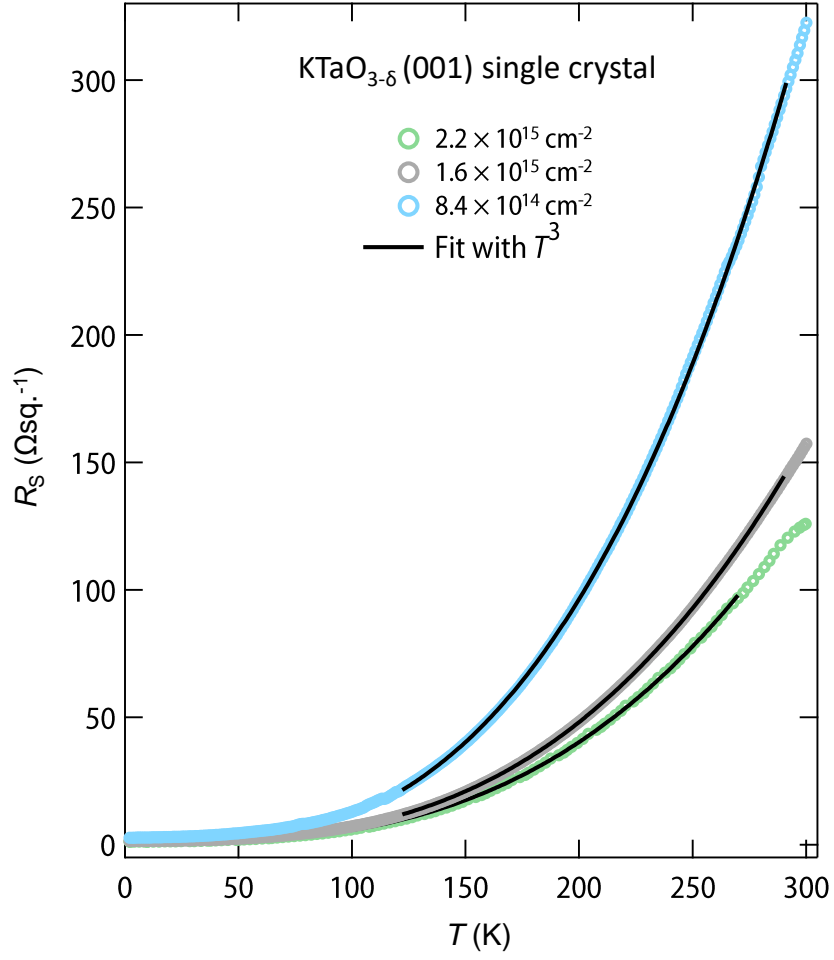


FIG. S2. Sheet resistance vs. temperature plot for three bulk oxygen deficient (001) oriented  $\text{KTaO}_3$  single crystal with sheet carrier densities  $2.2 \times 10^{15} \text{ cm}^{-2}$ ,  $1.6 \times 10^{15} \text{ cm}^{-2}$  and  $8.4 \times 10^{14} \text{ cm}^{-2}$  measured at room temperature. The solid black line denotes fitting with  $T^3$ . For more details about these samples we refer to our previous work [4, 5].

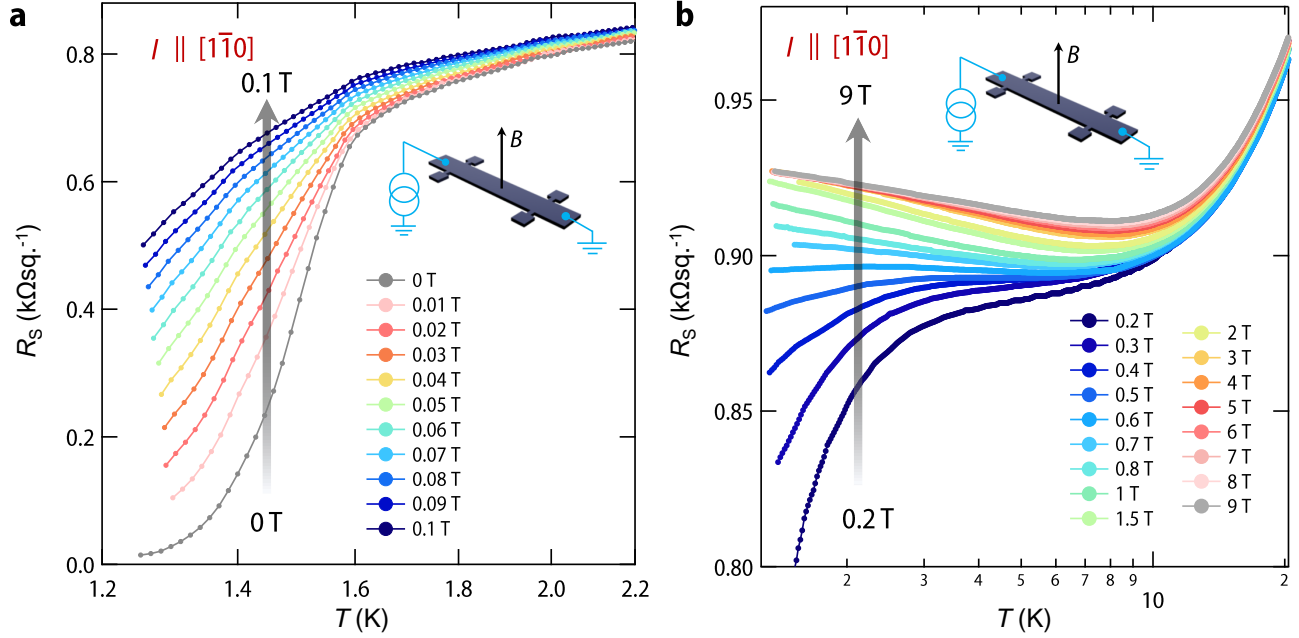


FIG. S3. Low temperature variation of  $R_S$  under  $B_{\perp}$  for the Hall bar along  $[1\bar{1}0]$  has been shown in **a.** (from 0 T to 0.1 T) and **b.** (from 0.2 T to 9 T) for 7 nm  $\text{AlO}_x/\text{KTaO}_3$  (111) sample. Similar to the Hall bar along  $[11\bar{2}]$ , an avoided superconductor insulator transition is observed around  $R_S \sim 0.9 \text{ k}\Omega\text{sq}^{-1}$ . A logarithmic dependence is also observed at higher  $B$  and low  $T$ .

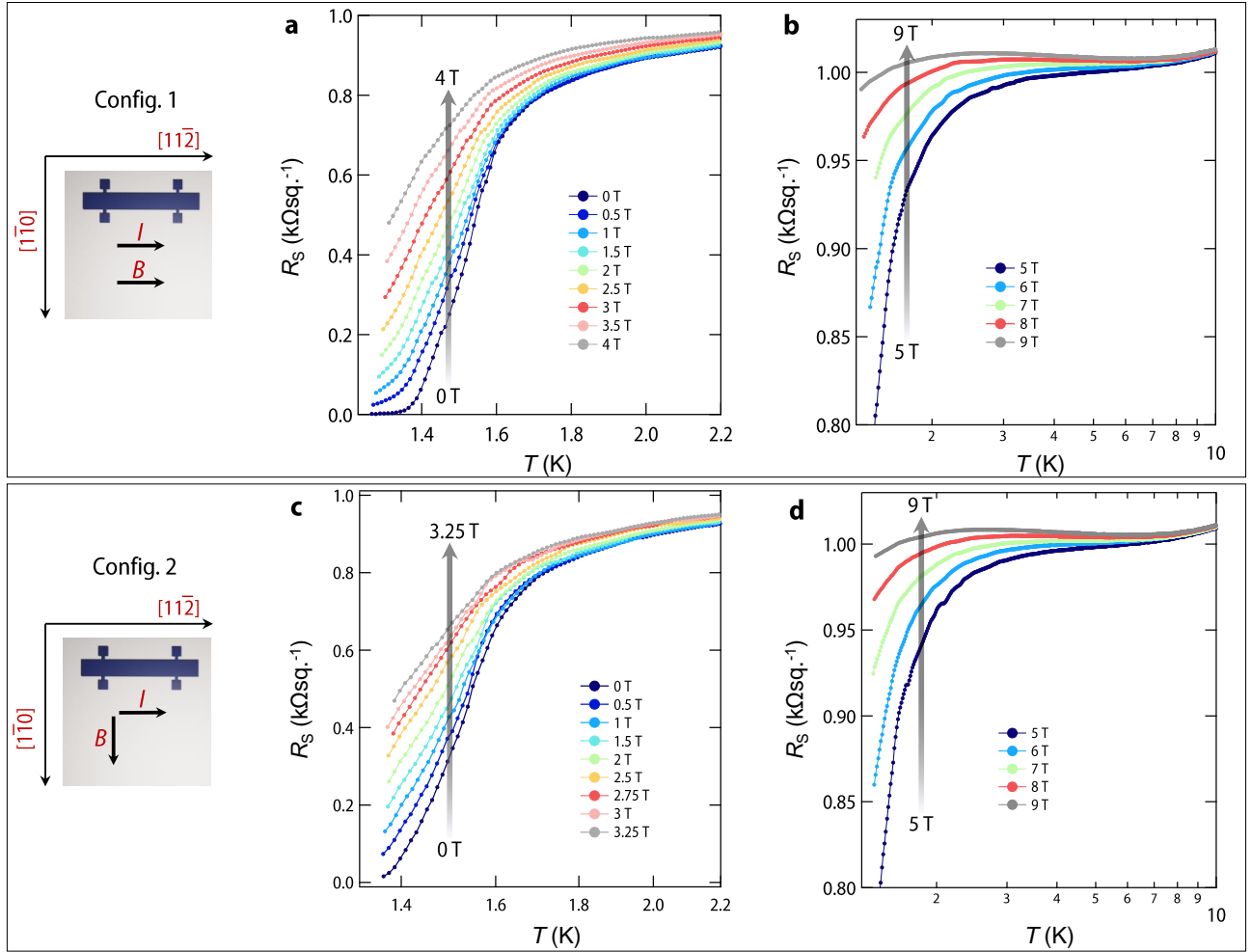


FIG. S4. Low temperature variation of  $R_S$  under  $B_{\parallel}$  (for  $7 \text{ nm AlO}_x/\text{KTaO}_3$  (111) sample) when  $I \parallel [11\bar{2}]$  and  $B \parallel I$  has been shown in **a.** (from 0 T to 4 T) and **b.** (from 5 T to 9 T). Plots for the case when  $I \parallel [11\bar{2}]$  and  $B \perp I$  has been shown in **c.** (from 0 T to 3.25 T) and **d.** (from 5 T to 9 T).

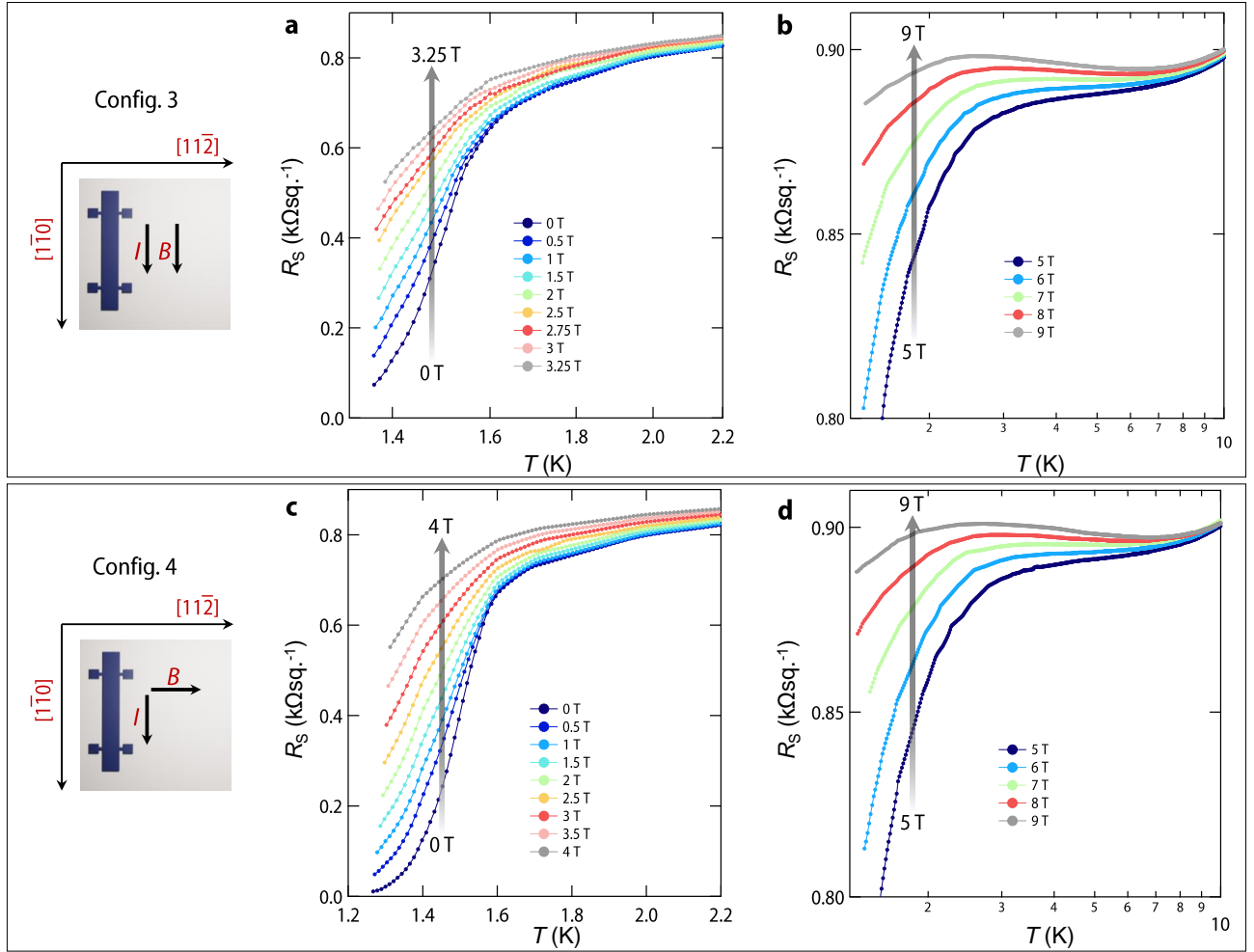


FIG. S5. (a) Low temperature variation of  $R_S$  under  $B_{\parallel}$  (for 7 nm  $\text{AlO}_x/\text{KTaO}_3$  (111) sample) when  $I \parallel [1\bar{1}0]$  and  $B \parallel I$  have been shown in **a.** (from 0 T to 3.25 T) and **b.** (from 5 T to 9 T). Plots for the case when  $I \parallel [11\bar{2}]$  and  $B \perp I$  has been shown in **c.** (from 0 T to 4 T) and **d.** (from 5 T to 9 T).

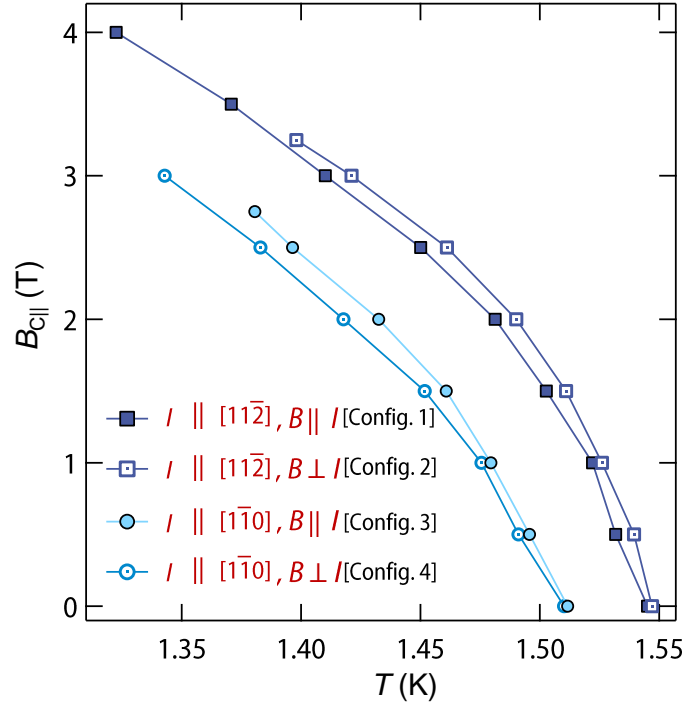
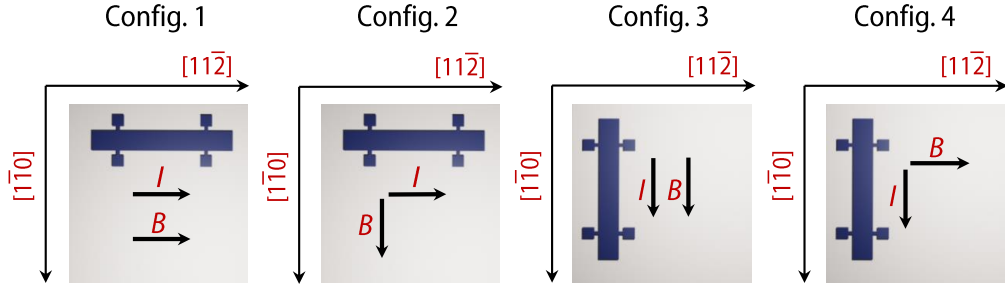


FIG. S6. Temperature dependent in-plane upper critical field ( $B_{C||}$ ), obtained by tracking the evolution of  $T_C$  with  $B_{||}$  in  $R_S$  vs.  $T$  plot for all the four configurations discussed in Supplementary Figs. 5 and 6. For the case of Hall bar along  $[11\bar{2}]$ ,  $B_{C||}$  is found to be lower for the case when  $B \parallel I$  (configuration 1) than  $B \perp I$  case (configuration 2). Interestingly, this trend is completely opposite for the Hall bar along  $[1\bar{1}0]$  where  $B_{C||}$  for the case when  $B \parallel I$  (configuration 3) is found to be higher than  $B \perp I$  case (configuration 4). Such a behavior could arise from a small  $p$ -wave component in the superconducting order parameter as proposed recently [6].

**Supplementary Note 2: Fitting of weak antilocalization data with Iordanskii, Lyanda-Geller, and Pikus theory**

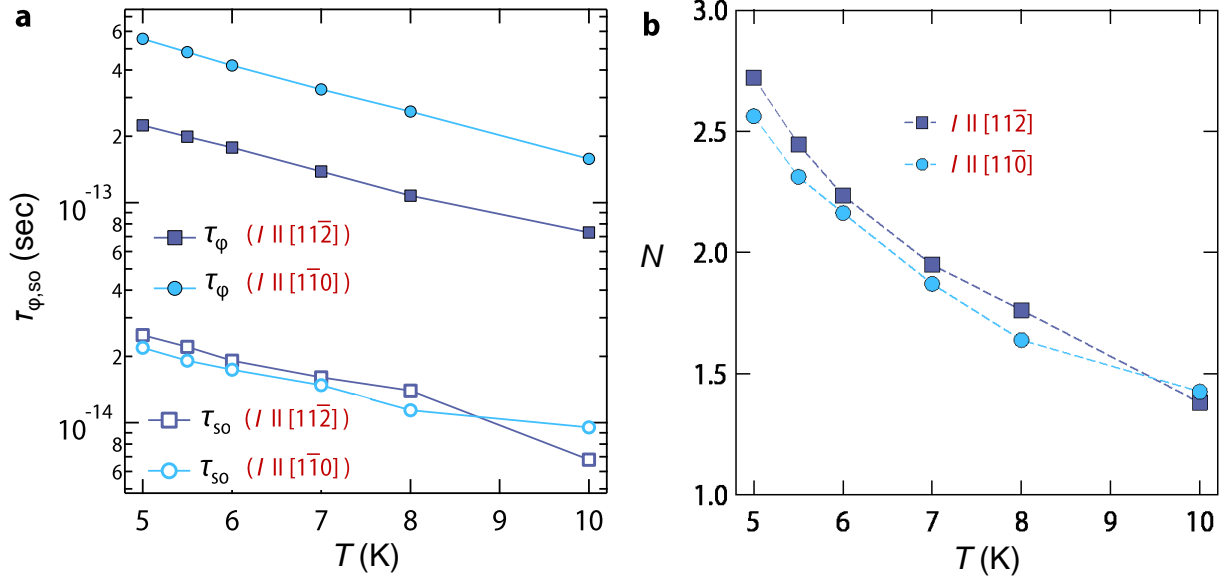


FIG. S7. **a.** Temperature dependence of the phase coherence time ( $\tau_\phi$ ) and spin precession time ( $\tau_{SO}$ ) obtained from the fitting for both the Hall bars. **b.** Temperature dependence of the number of independent channels contributing to weak antilocalization.

As shown in the main text, Iordanskii, Lyanda-Geller, and Pikus theory (with only cubic Rashba term) along with a small Kohler  $B^2$  term provides an excellent fit at all temperatures. In the absence of linear Rashba term, the correction to the sheet conductance ( $\Delta\sigma$ ) is given by

$$\begin{aligned} \Delta\sigma(B) = N \frac{e^2}{\pi h} & \left[ \Psi\left(\frac{1}{2} + \frac{B_\phi}{B} + \frac{B_{SO}}{B}\right) - \frac{1}{2} \Psi\left(\frac{1}{2} + \frac{B_\phi}{B}\right) \right. \\ & + \frac{1}{2} \Psi\left(\frac{1}{2} + \frac{B_\phi}{B} + 2\frac{B_{SO}}{B}\right) - \ln \frac{B_\phi + B_{SO}}{B} \\ & \left. - \frac{1}{2} \ln \frac{B_\phi + 2B_{SO}}{B} + \frac{1}{2} \ln \frac{B_\phi}{B} \right] \end{aligned} \quad (7)$$

where  $N$  is the number of independent interference channels [7],  $\Psi$  is the digamma function,  $B_\phi = \frac{\hbar}{4el_\phi^2}$  ( $l_\phi$  is the phase coherence length) and  $B_{SO} = \frac{\hbar}{4el_{SO}^2}$  ( $l_{SO}$  is the spin-precession length) where  $\hbar$  is the reduced Planck's constant. Associated characteristics time scales, phase coherence time ( $\tau_\phi$ ) and spin precession time ( $\tau_{SO}$ ) are given by  $\tau_\phi = \frac{\hbar}{4eDB_\phi}$  and  $\tau_{SO} = \frac{\hbar}{4eDB_{SO}}$  where  $D$  is the diffusion coefficient given by  $D = v_f^2 \tau / 2$  ( $v_f$  is the Fermi velocity and  $\tau$  is the elastic scattering time).

$v_f$  and  $\tau$  were estimated assuming a single band having parabolic dispersion with effective mass  $m^* = 0.3m_e$  [8]. Supplementary Figure S7a shows the temperature dependent  $\tau_\phi$  and  $\tau_{SO}$  obtained from the fitting for both the Hall bars along  $[11\bar{2}]$  and  $[1\bar{1}0]$ . As evident,  $\tau_{SO}$  is smaller than  $\tau_\phi$  satisfying the criteria for weak-anti localization [9, 10]. Temperature dependence of the number of independent channels has been plotted in Supplementary Figure S7b.



**Supplementary Note 3: Transverse resistance ( $R_{xy}$ ) as a function of the out-of-plane magnetic field at different temperatures**

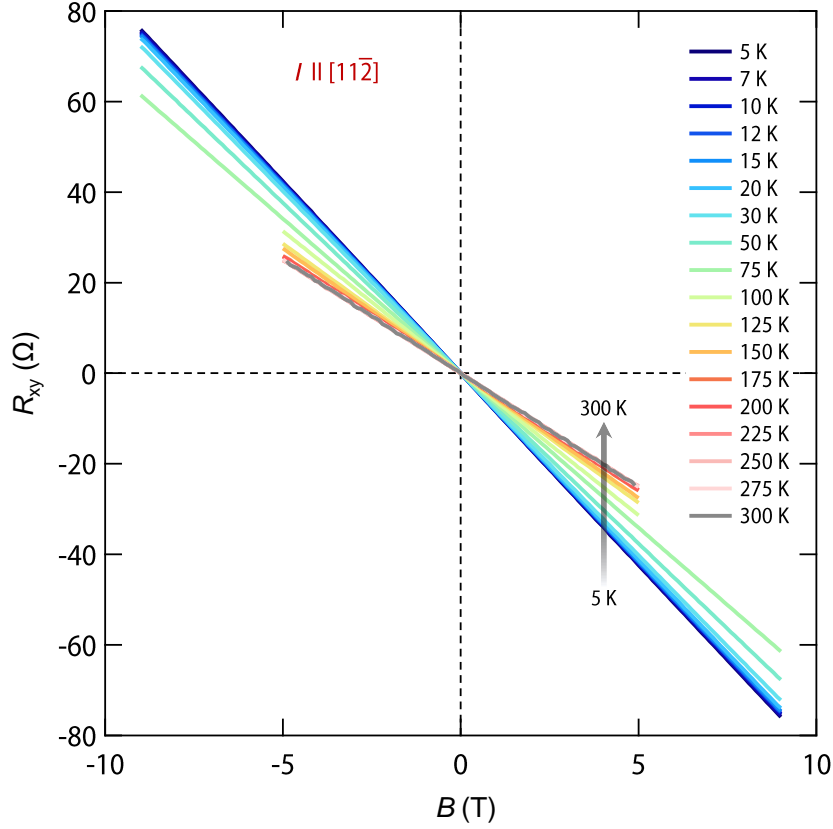


FIG. S8. Antisymmetrized transverse resistance as a function of the magnetic field measured at various temperatures in the metallic phase for 7 nm  $\text{AlO}_x/\text{KTaO}_3$  (111) sample. The direction of  $I$  is along the crystallographic axis  $[1\bar{1}2]$ .

Supplementary Figure S8 shows  $R_{xy}$  vs.  $B$  curves recorded at several fixed temperatures. To eliminate the longitudinal component of resistance ( $R_{xx}$ ), the data has been antisymmetrized with respect to  $B$ . As clearly evident, the slope  $R_{xy}/B$  increases with the decrease in temperature. Assuming single band transport, the Hall coefficient is given by  $R_H = -1/ne$  (where  $n$  is the carrier density and  $-e$  is the electron's charge). Since,  $R_{xy}/B = R_H$ , an increase in slope  $R_{xy}/B$  with lowering of temperature immediately suggests decreasing  $n$  with lowering of temperature. A similar trend has also been observed for other Hall bar along  $[1\bar{1}0]$ . In Supplementary Note 4 and 5, we discuss the origin of the nonlinear Hall effect in the present case.

### Supplementary Note 4: Non-linear Hall effect and evidence for two-band transport

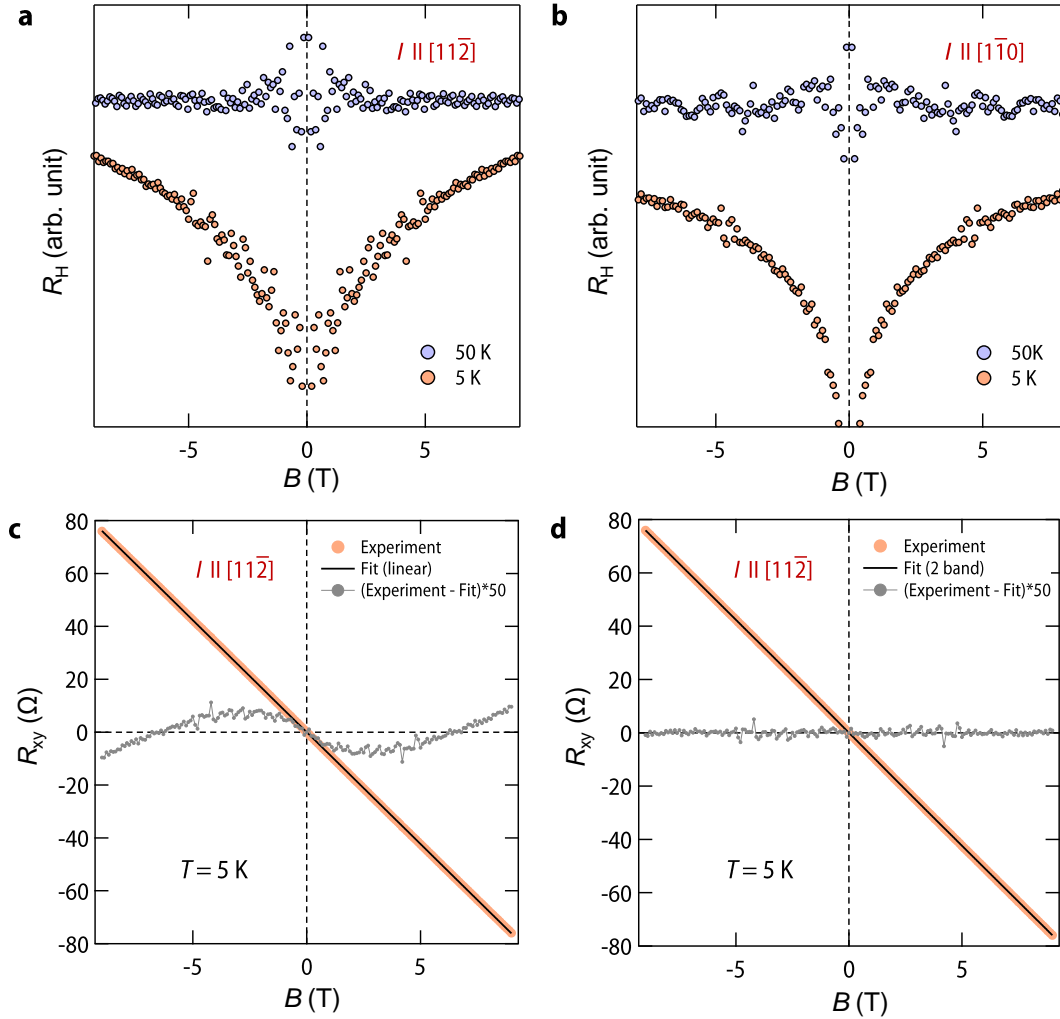


FIG. S9. The Hall coefficient  $R_H$  as a function of out-of-plane magnetic field at 5 K and 50 K for both the Hall bars along  $[11\bar{2}]$  and  $[1\bar{1}0]$  has been shown in **a** and **b**. **c**. Linear fitting of  $R_{xy}$  vs.  $B$  data at 5 K for  $I$  along  $[11\bar{2}]$ . To visualize the presence of little non-linearity in  $R_{xy}$ , the residual ( $R_{xy}$ -Fit) is multiplied by 50. **d**.  $R_{xy}$  vs.  $B$  data at 5 K (for  $I$  along  $[11\bar{2}]$ ) along with fitting using two band model.

To extract the value of  $n$ , we have tried to fit the data with a straight line assuming one band model. Interestingly, we find that, below 20 K,  $R_{xy}$  vs.  $B$  can not be captured using one band approximation due to the presence of a little non-linearity. This is clearly evident in the  $R_H$  vs.  $B$  plot shown in Supplementary Figure S9a and Supplementary Figure S9b for both the Hall bars. Supplementary Figure S9c shows the failure of one band model in describing our Hall data at 5 K. Such nonlinear effects in  $R_{xy}$  could arise from the presence of multi carrier transport at the

interface. In order to verify this, we have considered a minimal two band model where  $R_{xy}$  is given by

$$R_{xy} = -\frac{1}{e} \frac{\left(\frac{n_1\mu_1^2}{1+\mu_1^2B^2} + \frac{n_2\mu_2^2}{1+\mu_2^2B^2}\right)B}{\left(\frac{n_1\mu_1}{1+\mu_1^2B^2} + \frac{n_2\mu_2}{1+\mu_2^2B^2}\right)^2 + \left(\frac{n_1\mu_1^2}{1+\mu_1^2B^2} + \frac{n_2\mu_2^2}{1+\mu_2^2B^2}\right)^2B^2} \quad (8)$$

with the constraint  $(e.R_S)^{-1} = n_1\mu_1 + n_2\mu_2$ . Here,  $n_1$ ,  $n_2$  and  $\mu_1$ ,  $\mu_2$  are the sheet carrier densities and mobilities of the two types of electrons. As evident from the Supplementary Figure S9d, two band model provides an excellent fit to our Hall data in the whole range of  $B$  strongly indicating the presence of two types of carriers in the system. Such a two band transport has not been demonstrated so far for KTaO<sub>3</sub> (111) based superconductors.

**Supplementary Note 5: Temperature dependent sheet carrier density ( $n_S$ ), mobility ( $\mu$ ) and evidence for carrier freezing effect**

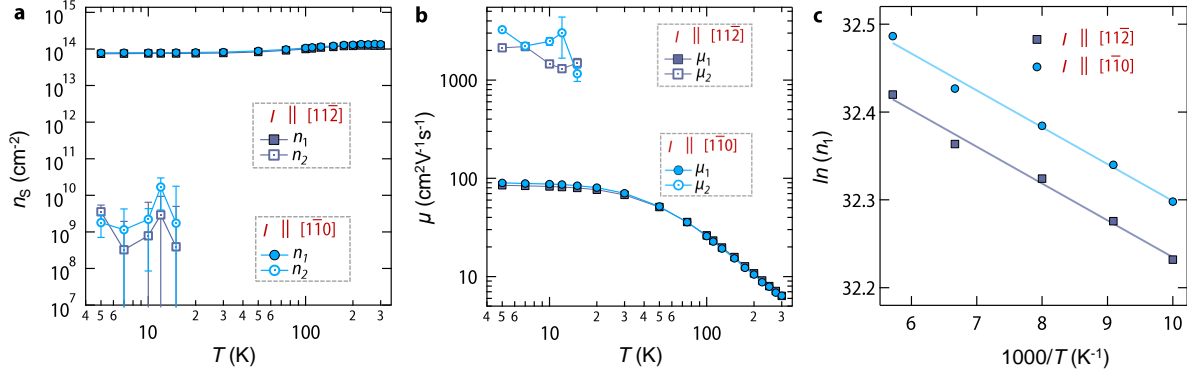


FIG. S10. **a.** Temperature dependent  $n_S$  (for Hall bar along  $[11\bar{2}]$  and  $[1\bar{1}0]$ ) obtained from fitting of anti-symmetrized  $R_{xy}$ .  $n_1$  and  $n_2$  are the density of electrons confined to the lower and upper band, respectively. **b.** Temperature dependent mobility ( $\mu$ ) for Hall bar along  $[11\bar{2}]$  and  $[1\bar{1}0]$ .  $\mu_1$  and  $\mu_2$  are electron's mobility confined to the lower and upper band, respectively. **c.** The Arrhenius plot of  $\ln(n_1)$  for the temperature range 100 K–175 K for both the Hall bars.

Supplementary Figure S10a shows temperature dependent  $n_1$  and  $n_2$  obtained for  $I$  along  $[11\bar{2}]$  and  $[1\bar{1}0]$ . Surprisingly,  $n_2$  is found out to be  $\sim 10^9$  cm<sup>-2</sup> which is 5 orders of magnitude lower than  $n_1$ . Supplementary Figure S10b shows the corresponding variation of mobility. The mobility of low density carriers ( $\mu_2$ ) is found to be higher than that of high density carriers ( $\mu_1$ ). Interestingly, a prominent carrier freezing effect [11] is observed below 175 K down to 100 K. This is evident from the Arrhenius plot of  $\ln(n_1)$  vs.  $1000/T$  shown in the Supplementary Figure S10c. A linear fit results in a very shallow defect state, which would be just 3.6 meV below the conduction band.

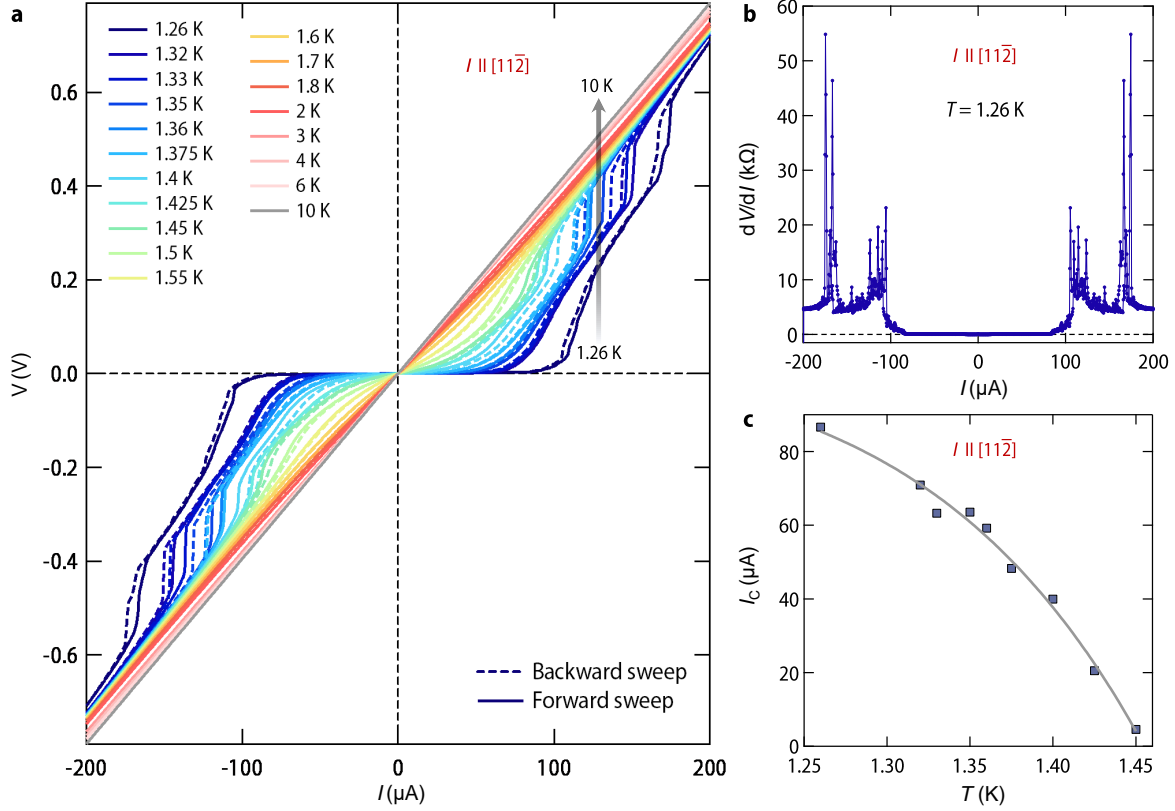


FIG. S11. **a.** Temperature dependent full cycle  $I$ - $V$  curves measured in current bias mode for the Hall bar along  $[11\bar{2}]$  on 7 nm  $\text{AlO}_x/\text{KTaO}_3$  (111) sample. For full cycle measurement, the current was swept from  $0 \mu\text{A} \rightarrow 200 \mu\text{A} \rightarrow -200 \mu\text{A} \rightarrow 200 \mu\text{A} \rightarrow 0 \mu\text{A}$ . For the sake of clarity,  $0 \mu\text{A} \rightarrow 200 \mu\text{A}$  and  $200 \mu\text{A} \rightarrow 0 \mu\text{A}$  branches have not been shown in the plot.  $200 \mu\text{A} \rightarrow -200 \mu\text{A}$  branch is denoted as backward sweep and  $-200 \mu\text{A} \rightarrow 200 \mu\text{A}$  branch is denoted as forward sweep. **b.**  $dV/dI$  plot at 1.26 K for  $I$  along  $[11\bar{2}]$ . Several spikes in the derivative above certain current correspond to several discrete jumps in the voltage drop. **d.** Temperature dependence of critical current ( $I_C$ ).

### Supplementary Note 6: Effect of self-field generated due to applied current in the sample

In order to check the impact of magnetic field generated due to the applied current in the sample we have estimated its order of magnitude following the results described in the reference [12]. Since the in-plane component of the magnetic field would have null effect on the vortices, we have only estimated the out of plane component. In the Supplementary Figure S12b we have plotted the variation of the out of plane component of the magnetic field ( $B_y$ ) across the sample width within the superconducting strip (for sample geometry see Supplementary Figure S12a). As evident,  $B_y$  peaks at edges of the sample boundary and has the maximum value of  $\sim 3\mu_0 b J_p / \pi$ , where  $\mu_0$  is the permeability of vacuum and  $J_p$  is pair breaking current density. Using the parameters for our sample, the obtained value of  $(B_y)_{max}$  at 1.26 K for 7 nm  $\text{AlO}_x/\text{KTaO}_3$  (111) sample for Hall bar along  $[11\bar{2}]$  would be  $\sim 10^{-8}$  Tesla (for the sake of simplicity we have taken the value of pair breaking current just after the voltage instability). We now move one step further to back calculate the critical vortex velocity required to produce a LO type voltage instability with a magnetic field of  $\sim 10^{-8}$  Tesla by using the formula  $V^* = v^* BL$  where  $L$  is the length between the voltage probes. Putting the value of  $V^*$  and  $L$  yields a gigantically large value of  $v^* \sim 10^{10} \text{ ms}^{-1}$ . This is two orders of magnitude higher than the speed of the light and hence is unphysical, emphasizing that self-field generated due to the applied current in the system would be insufficient to lead to LO type instability.

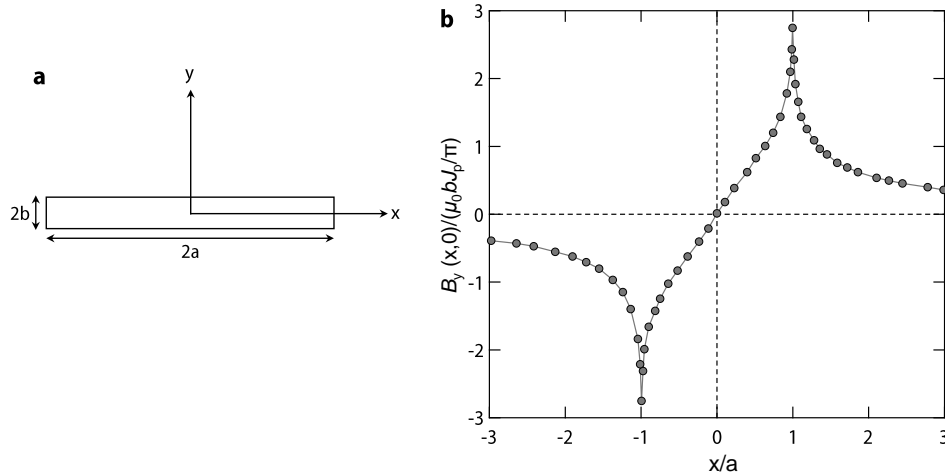


FIG. S12. **a.** Geometry of the superconducting strip where width of the strip is  $2a$  and the thickness is  $2b$ . In this geometry current is sent along the  $z$ -axis which is perpendicular to  $x$  and  $y$  axes. **b.** Out of plane component of the magnetic field along the  $x$ -axis for  $y=0$ . This plot has been reproduced with permission by digitising the 3<sup>rd</sup> figure of the reference [12].

### Supplementary Note 7: Effect of residual field in the magnet

While we have followed the standard protocol to bring down the magnetic field to zero by oscillating the field, there is always a possibility of very small residual field during the measurement. In order to completely get rid of residual field in our system, we have purposely warmed our superconducting magnet (Oxford Instruments) to room temperature and we waited at room temperature for two weeks to make sure complete evaporations of all cryogenics (liquid helium, liquid nitrogen) from the system. This makes sure that there is no residual field present in the magnet. Thereafter the system was freshly precooled, and  $I$ - $V$  measurements were performed without applying any magnetic field. In Supplementary Figure S13 we show the comparison of  $I$ - $V$  data recorded at one representative temperature (1.46 K) for 14 nm  $\text{AlO}_x$  film on  $\text{KTaO}_3$  (111) ( $I$  along  $[11\bar{2}]$ ) before and after warming the magnet. As evident curves look same, signifying that residual field in the measurement setup has no role for our observation.

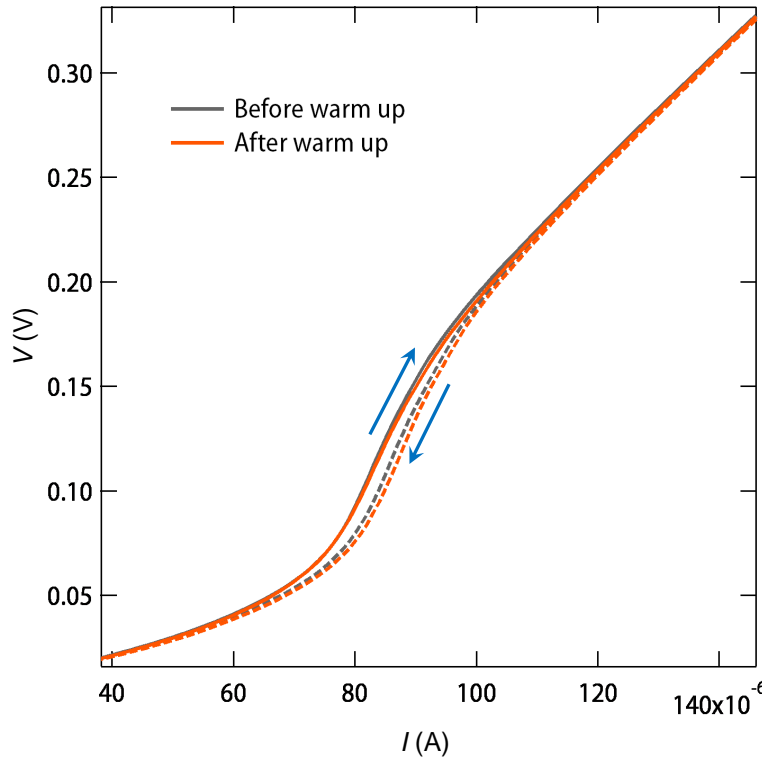


FIG. S13.  $I$ - $V$  characteristics recorded at 1.46 K for 14 nm  $\text{AlO}_x/\text{KTaO}_3$  (111) sample ( $I$  along  $[11\bar{2}]$ ) before and after warming the magnet.

### Supplementary Note 8: Vortex velocity calculation in absence of magnetic field.

According to the Gor'kov–Josephson relation [13, 14], the expression for voltage drop is given by

$$V = n_f \Phi_0 v L \quad (9)$$

where  $n_f$  is the free vortex density,  $\Phi_0$  is the magnetic flux quantum and  $L$  is the distance between voltage probes. This expression is markedly distinct from the bulk type II superconductors where  $V$  under perpendicular magnetic field is given by  $V = v B L$ . This basic difference emerges from the fact that in bulk type II superconductors the  $n_f$  is decided by just the magnitude of  $B$  and hence  $V$  is independent of temperature and current, which is not the case in 2D superconductors as discussed earlier. In the following we first discuss the steps followed to calculate  $n_f$  at a given temperature and current across BKT transition in absence of  $B$ :

(i) Case I ( $I \rightarrow 0$  limit): At absolute zero current and below  $T_{\text{BKT}}$ , vortex and antivortex always exist as bound pairs and hence the resistance should be zero as there are no free vortices. However, application of how so ever small current always leads to Ohmic dissipation in  $I \rightarrow 0$  limit due to breaking of few weakly bound vortex-antivortex pairs [15] as discussed in main text.

Between  $T_{\text{BKT}} \leq T \leq T_{\text{C}}$ , thermal fluctuation leads to breaking of vortex-antivortex pairs interacting at a distance  $r$  larger than the correlation length ( $\xi_v$ ) and bound pairs still exist for  $r < \xi_v$ . In order to calculate  $n_f$  in  $I \rightarrow 0$  limit we use the following universal relation [15]

$$R = R_{\text{N}} 2\pi \xi^2 n_f \quad (10)$$

where  $R_{\text{N}}$  is the normal state resistance. For estimating  $R$ , we fit the  $I$ - $V$  curve from 0-10  $\mu\text{A}$  with Ohm's law where the  $I$ - $V$  curve is indeed linear. The obtained resistance is then plugged in Supplementary equation 10 along with  $R_{\text{N}}$  at 5 K and  $n_f$  is back calculated. For estimation of  $\xi$  we use the relation  $\xi(T) = \xi(0)(1-T/T_{\text{C}})^{-1/2}$ . We denote the  $n_f$  estimated in  $I \rightarrow 0$  limit by  $n_{f0}$ .

(ii) Case II ( $I^\alpha$  regime): This corresponds to non-Ohmic regime where a power law dependence is observed due to breaking of vortex-antivortex bound pairs. This introduces additional vortices at higher currents which is given by  $n_{\text{fp}} = K I^{\alpha-1}$  where  $\alpha$  is the same power factor as discussed in Fig. 3c of the main text and  $K$  is the temperature dependent coefficient which is estimated from the following relation [16]



$$V = 2\pi\xi^2 K R_N I^\alpha \quad (11)$$

by fitting the  $I$ - $V$  curve in power law regime. Since the voltage instability occurs well beyond the  $I^\alpha$  regime, the total  $n_f$  in absence of  $B$  is given by  $n_f = n_{f0} + n_{fp}$ . This value is then put in Supplementary equation 9 and the vortex velocity is back calculated.

**Supplementary Note 9: Derivation for temperature dependence of LO instability in BKT system and effect of self-heating.**

Another successful prediction of LO theory has been the temperature dependence of  $v^*$  close to  $T_C$  given by  $v^* \propto \Delta^{1/2} \propto (1-T/T_C)^{1/4}$ . However, this relation was derived with the constraint that  $n_f$  is independent of temperature which is not the case in 2D superconductors. In the following we first derive the relevant expression of  $v^*$  in context of BKT system. For this we follow the approach described in ref [17] which predicts the following relation for  $\eta(v)$

$$\eta(v) = \eta(0) - \eta(0) \frac{\delta E}{\Delta} \quad (12)$$

where  $\delta E/\Delta$  is the fraction of quasiparticles that have left the vortex core due to  $\delta E$  change in the average quasiparticle energy due to electric field from flux-flow. Considering the balance between viscous damping force and Lorentz force along with the Supplementary equation 9 yields  $\delta E = \eta(v) v^2 n_f \tau_e / n_{qp}$  where  $n_{qp}$  is the quasiparticle density in vortex core and  $\tau_e$  is the electron's inelastic scattering time. Putting this relation in Supplementary equation 12, we recover the expression for LO theory given in equation 3 of the main text. Considering the expression  $\eta(0) = \phi_0^2 d / 2\pi \xi^2 R_N$  from Bardeen-Stephen law [16, 18] we obtain the expression for  $v^*$  as

$$v^* = \left( \frac{2\pi R_N n_{qp} \Delta(T) \xi^2(T)}{\phi_0^2 d \tau_e n_f(T, B)} \right)^{1/2} \quad (13)$$

We note that, this relation is drastically different from the LO theory where the temperature dependence enters only through  $\Delta$ . Further, considering the Bezuglyj and Shklovskij model for effect of self-heating on FFI near  $T_C$  would lead to additional  $B^{-1/2}$  dependence [19, 20], modifying the Supplementary equation 13 to

$$v^* = k \left( \frac{2\pi R_N n_{qp} \Delta(T) \xi^2(T)}{\phi_0^2 d \tau_e n_f(T, B)} \right)^{1/2} B^{-1/2} \quad (14)$$

where  $k$  is a constant.

**Supplementary Note 10: Calculation of  $n_f \xi^2$ .**

(i) In the absence of magnetic field, the value  $n_f \xi^2$  before the voltage instability would be given by  $n_f \xi^2 = n_{f0} \xi^2 + n_{fp} \xi^2$ .  $n_{f0} \xi^2$  is calculated using Supplementary equation 10 as discussed earlier and  $n_{fp} \xi^2$  is given by  $n_{fp} \xi^2 = K \xi^2 I^{\alpha-1}$ . The product  $K \xi^2$  is estimated from the Supplementary equation 11 and the value of  $I$  is taken at the mid of power law region in the  $I$ - $V$  measurement.

(ii) Application of  $B$  leads to an imbalance between vortex and antivortex by increasing the concentration of one of the species by an amount  $n_{fB}$  [21]. This leads to an additional resistance which we capture by fitting  $I$ - $V$  curve (at a fixed  $B$ ) in low current regime ( $0 \mu\text{A}$  to  $10 \mu\text{A}$ ) with Ohm's law. The  $n_{fB} \xi^2$  is then calculated using Supplementary equation 10 where the value of  $R_N$  is taken at 5 K. The total  $n_f \xi^2$  in presence of magnetic field is then given by  $n_f \xi^2 = n_{f0} \xi^2 + n_{fp} \xi^2 + n_{fB} \xi^2$ .

## Supplementary Note 11: Temperature dependence of LO instability across BKT transition

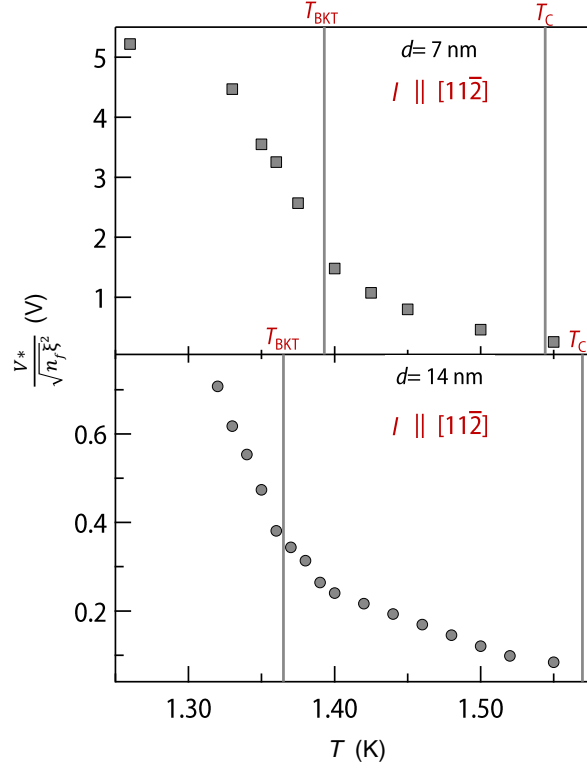


FIG. S14. Temperature evolution of normalized critical voltage calculated for Hall bar along  $[11\bar{2}]$  for 7 nm and 14 nm  $\text{AlO}_x/\text{KTaO}_3$  (111) samples.

The temperature dependence of normalized  $V^*$  ( $V^*/\sqrt{n_f \xi^2}$ ) for two samples on Hall bars along  $[11\bar{2}]$  has been shown in Supplementary Figure S14. As evident, the curves do not follow the  $(1-T/T_C)^{1/4}$  dependence considering  $\Delta \propto (1-T/T_C)^{1/2}$ . Further, we also observe an appreciable enhancement in the normalized  $V^*$  below  $T_{\text{BKT}}$ . We propose that such a peculiar behavior could arise due to the dominant role of hot-spot effect below  $T_{\text{BKT}}$  [22] which would lead to overestimation of  $V^*$ , whereas LO instability would be more applicable near  $T_C$  [23]. We note that a similar inference was drawn earlier on  $\text{YBa}_2\text{Cu}_3\text{O}_{7-\delta}$  films where LO instability was observed along with hot-spots [24].

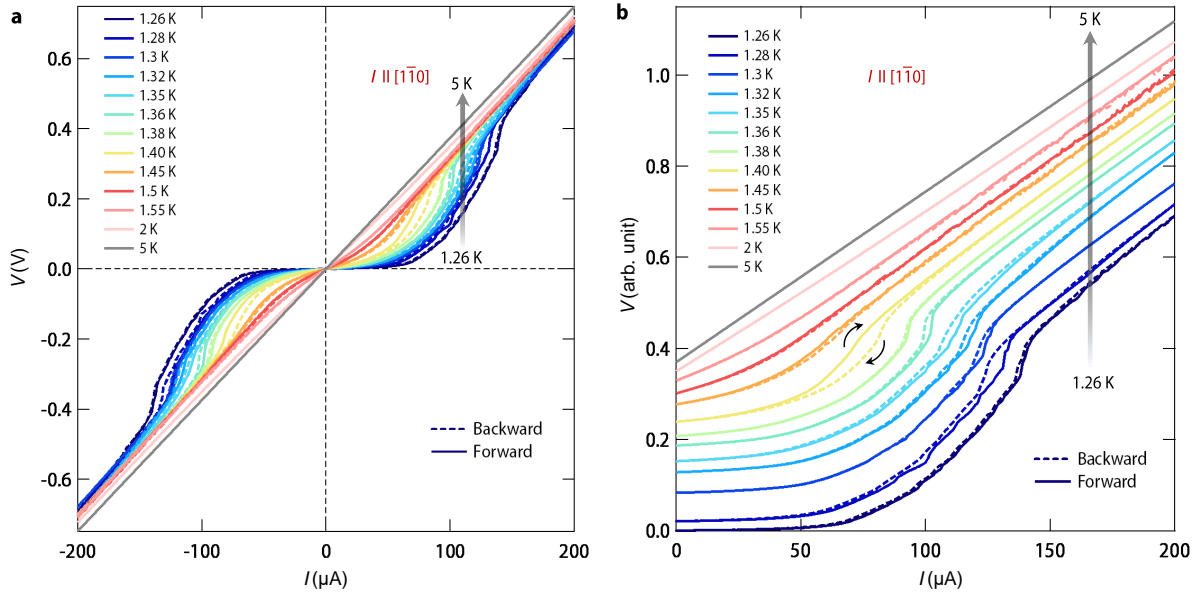


FIG. S15. **a**. Temperature dependent full cycle  $I$ - $V$  curves measured in current bias mode for the Hall bar along  $[1\bar{1}0]$  on  $7 \text{ nm AlO}_x/\text{KTaO}_3 (111)$  sample. For the sake of clarity,  $0 \mu\text{A} \rightarrow 200 \mu\text{A}$  and  $200 \mu\text{A} \rightarrow 0 \mu\text{A}$  branches have not been shown in the plot. Figure **b** shows the same plot with all the curves (except at 1.26 K) shifted vertically for visual clarity. Similar to  $I$  along  $[11\bar{2}]$ , clockwise hysteresis appears above a certain temperature.

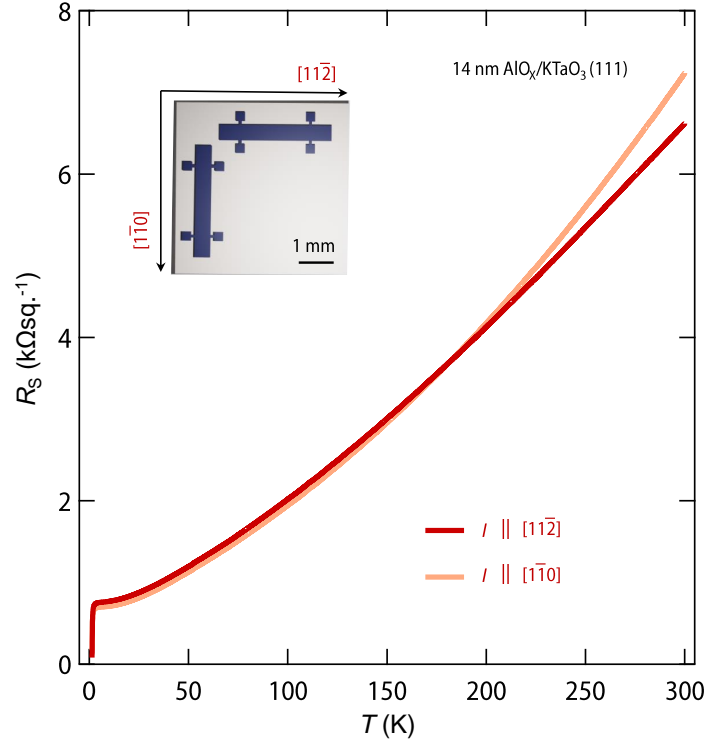


FIG. S16. Temperature dependent  $R_S$  of another sample with 14 nm  $\text{AlO}_x$  thickness. Similar to 7 nm  $\text{AlO}_x/\text{KTaO}_3$  (111) sample, a little anisotropy is observed between Hall bars made along  $[11\bar{2}]$  and  $[1\bar{1}0]$ .  $T_C$  is found to be 1.57 K and 1.51 K for current along  $[11\bar{2}]$  and  $[1\bar{1}0]$ , respectively.

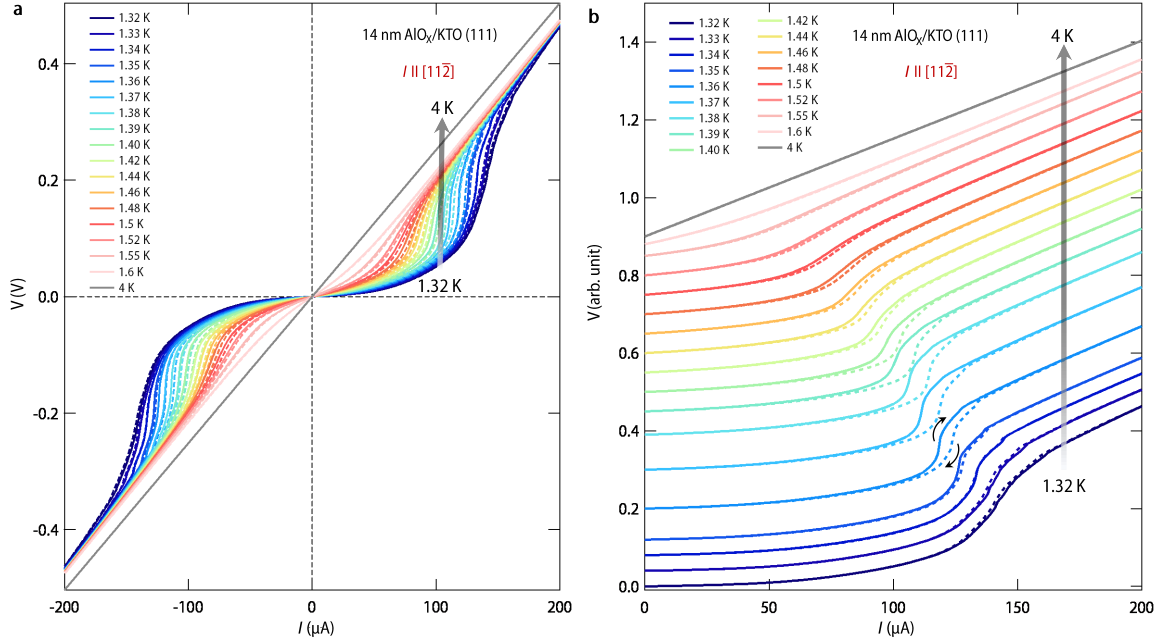


FIG. S17. **a** Temperature dependent full cycle  $I$ - $V$  curves measured in current bias mode ( $I \parallel [11\bar{2}]$ ) on another sample with 14 nm  $\text{AlO}_x$  thickness. For the sake of clarity,  $0 \mu\text{A} \rightarrow 200 \mu\text{A}$  and  $200 \mu\text{A} \rightarrow 0 \mu\text{A}$  branches have not been shown in the plot. Figure **b** shows the same plot with all the curves (except at 1.26 K) shifted vertically for visual clarity. Similar to 7 nm  $\text{AlO}_x/\text{KTaO}_3$  (111) sample, clockwise hysteresis appears above  $T_{\text{BKT}}$ .

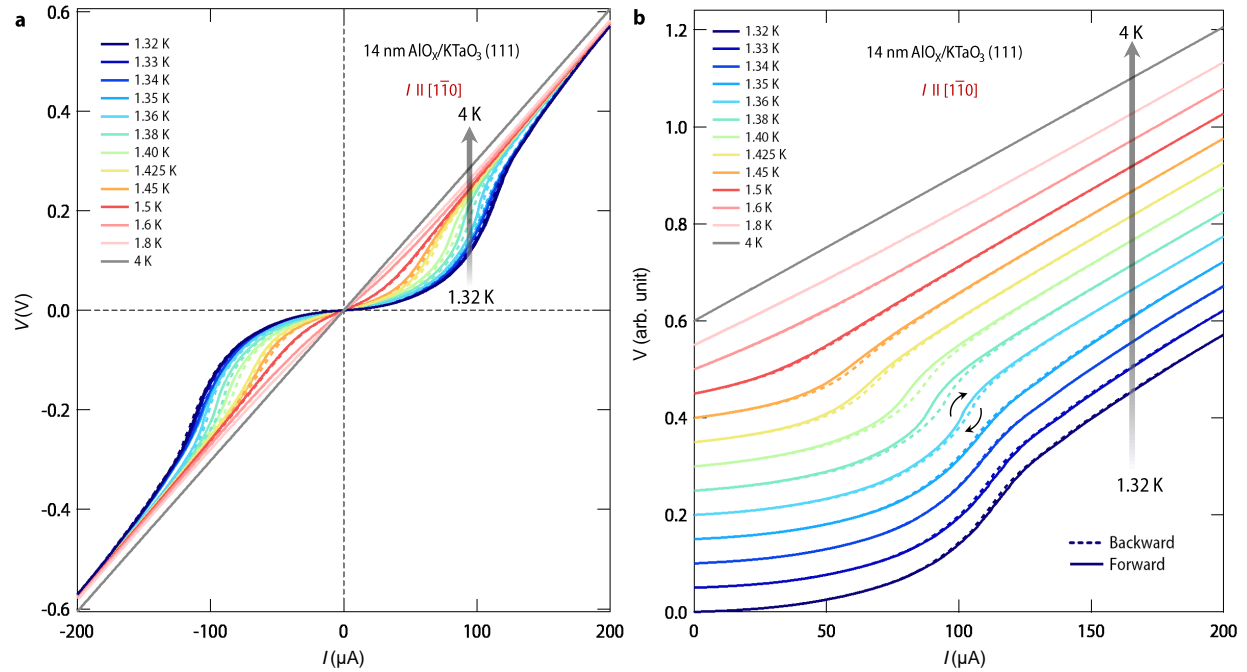


FIG. S18. **a.** Temperature dependent full cycle  $I$ - $V$  curves measured in current bias mode for the Hall bar along  $[1\bar{1}0]$  on another sample with  $14 \text{ nm AlO}_x$  thickness. For the sake of clarity,  $0 \mu\text{A} \rightarrow 200 \mu\text{A}$  and  $200 \mu\text{A} \rightarrow 0 \mu\text{A}$  branches have not been shown in the plot. Fig. **b** shows the same plot with all the curves (except at  $1.26 \text{ K}$ ) shifted vertically for visual clarity. Similar to  $I$  along  $[11\bar{2}]$ , clockwise hysteresis appears above  $T_{\text{BKT}}$ .



**Supplementary Note 12: Thermally activated flux flow above BKT transition.**

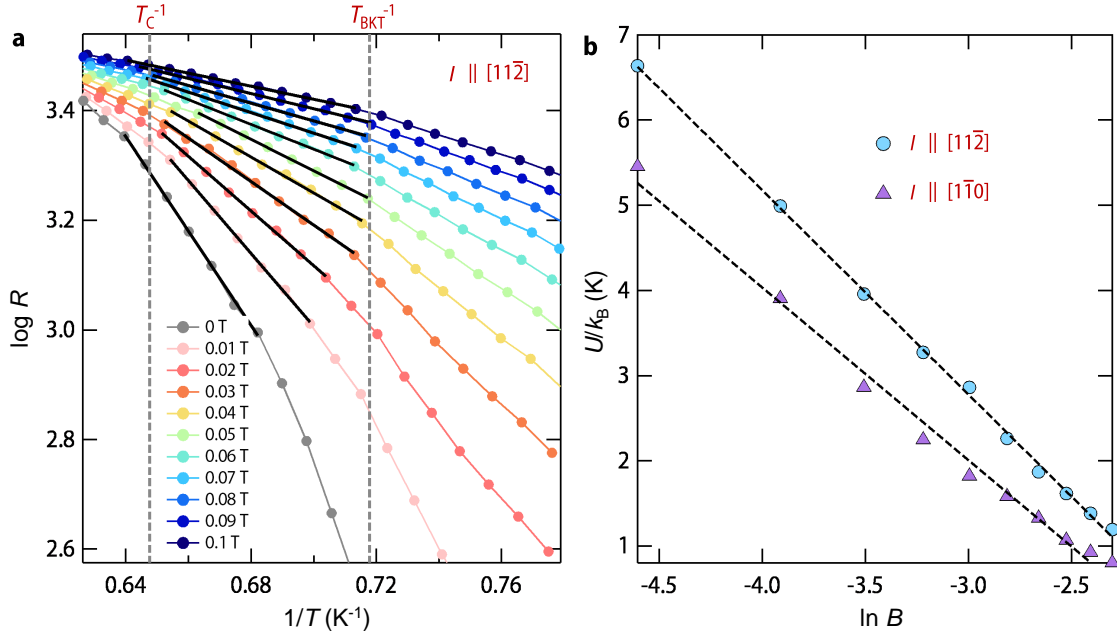


FIG. S19. **a.** Arrhenius plot of resistance at several fixed  $B$  for 7 nm  $\text{AlO}_x/\text{KTaO}_3$  sample (for Hall bar along  $[11\bar{2}]$ ). Solid black lines denote fitting with straight line. A similar behavior was observed for the Hall bar along  $[1\bar{1}0]$  (data not shown). **a.** Magnetic field dependent energy barrier ( $U$ ) extracted from the linear fit to the activated region for both the Hall bars.

As discussed in the main text, there is an abundance of free vortices above  $T_{\text{BKT}}$  which leads to the dissipation in presence of current due to the flux flow. This phenomena happens over an energy barrier ( $U$ ) and has activated behavior leading to the Arrhenius behavior ( $R \propto \exp(-U/k_B T)$ ) in the temperature range  $T_{\text{BKT}}$  and  $T_C$  as shown in the Supplementary Figure S19a. The extracted  $U$  from the fitting follows the expected dependence on the magnetic field  $U \propto \ln B$  (see Supplementary Figure S19b) [25].

---

**SUPPLEMENTARY REFERENCES**

- [1] Ichimiya, A., Cohen, P. I. & Cohen, P. I. *Reflection high-energy electron diffraction* (Cambridge University Press, 2004).
- [2] Middey, S. *et al.* Epitaxial growth of (111)-oriented  $\text{LaAlO}_3/\text{LaNiO}_3$  ultra-thin superlattices. *Ap-*

- plied Physics Letters* **101**, 261602 (2012). URL <https://doi.org/10.1063/1.4773375>.  
<https://doi.org/10.1063/1.4773375>.
- [3] Björck, M. & Andersson, G. Genx: an extensible x-ray reflectivity refinement program utilizing differential evolution. *Journal of Applied Crystallography* **40**, 1174–1178 (2007).
- [4] Ojha, S. K. *et al.* Oxygen vacancy-induced topological hall effect in a nonmagnetic band insulator. *Advanced Quantum Technologies* **3**, 2000021 (2020). URL <https://doi.org/10.1002/qute.202000021>.
- [5] Ojha, S. K. *et al.* Oxygen vacancy induced electronic structure modification of  $\text{KTaO}_3$ . *Phys. Rev. B* **103**, 085120 (2021). URL <https://link.aps.org/doi/10.1103/PhysRevB.103.085120>.
- [6] Zhang, G. *et al.* Spontaneous rotational symmetry breaking in  $\text{KTaO}_3$  interface superconductor. *arXiv preprint arXiv:2111.05650* (2021).
- [7] Nakamura, H. *et al.* Robust weak antilocalization due to spin-orbital entanglement in dirac material  $\text{Sr}_3\text{SnO}$ . *Nature Communications* **11**, 1161 (2020). URL <https://doi.org/10.1038/s41467-020-14900-1>.
- [8] Bareille, C. *et al.* Two-dimensional electron gas with six-fold symmetry at the (111) surface of  $\text{KTaO}_3$ . *Scientific Reports* **4**, 3586 (2014). URL <https://doi.org/10.1038/srep03586>.
- [9] Bergmann, G. Weak localization in thin films: a time-of-flight experiment with conduction electrons. *Physics Reports* **107**, 1–58 (1984). URL <https://www.sciencedirect.com/science/article/pii/0370157384901030>.
- [10] Caviglia, A. D. *et al.* Tunable rashba spin-orbit interaction at oxide interfaces. *Phys. Rev. Lett.* **104**, 126803 (2010). URL <https://link.aps.org/doi/10.1103/PhysRevLett.104.126803>.
- [11] Liu, Z. Q. *et al.* Metal-insulator transition in  $\text{SrTiO}_{3-x}$  thin films induced by frozen-out carriers. *Phys. Rev. Lett.* **107**, 146802 (2011). URL <https://link.aps.org/doi/10.1103/PhysRevLett.107.146802>.
- [12] Babaei Brojeny, A. A. & Clem, J. R. Self-field effects upon the critical current density of flat superconducting strips. *Superconductor Science and Technology* **18**, 888 (2005). URL <https://dx.doi.org/10.1088/0953-2048/18/6/016>.
- [13] Josephson, B. D. Supercurrents through barriers. *Advances in Physics* **14**, 419–451 (1965). URL <https://doi.org/10.1080/00018736500101091>.

- [14] Halperin, B. I. & Nelson, D. R. Resistive transition in superconducting films. *Journal of Low Temperature Physics* **36**, 599–616 (1979). URL <https://doi.org/10.1007/BF00116988>.
- [15] Jos, J. V. *40 Years of Berezinskii-Kosterlitz-Thouless Theory* (World Scientific, 2013).
- [16] Saito, Y., Itahashi, Y. M., Nojima, T. & Iwasa, Y. Dynamical vortex phase diagram of two-dimensional superconductivity in gated MoS<sub>2</sub>. *Phys. Rev. Materials* **4**, 074003 (2020). URL <https://link.aps.org/doi/10.1103/PhysRevMaterials.4.074003>.
- [17] Klein, W., Huebener, R. P., Gauss, S. & Parisi, J. Nonlinearity in the flux-flow behavior of thin-film superconductors. *Journal of Low Temperature Physics* **61**, 413–432 (1985). URL <https://doi.org/10.1007/BF00683694>.
- [18] Tinkham, M. *Introduction to superconductivity* (Courier Corporation, 2004).
- [19] Bezuglyj, A. I. & Shklovskij, V. A. Effect of self-heating on flux flow instability in a superconductor near  $T_C$ . *Physica C: Superconductivity* **202**, 234–242 (1992). URL <https://www.sciencedirect.com/science/article/pii/0921453492901659>.
- [20] Dobrovolskiy, O. V. *et al.* Ultra-fast vortex motion in a direct-write Nb-C superconductor. *Nature Communications* **11**, 3291 (2020). URL <https://doi.org/10.1038/s41467-020-16987-y>.
- [21] Doniach, S. & Huberman, B. A. Topological excitations in two-dimensional superconductors. *Phys. Rev. Lett.* **42**, 1169–1172 (1979). URL <https://link.aps.org/doi/10.1103/PhysRevLett.42.1169>.
- [22] Ovadyahu, Z. Transition to zero vorticity in a two-dimensional superconductor. *Phys. Rev. Lett.* **45**, 375–378 (1980). URL <https://link.aps.org/doi/10.1103/PhysRevLett.45.375>.
- [23] Larkin, A. & Ovchinnikov, Y. Nonlinear conductivity of superconductors in the mixed state. *Sov. Phys. JETP* **41**, 960–965 (1975).
- [24] Xiao, Z. L., Andrei, E. Y. & Ziemann, P. Coexistence of the hot-spot effect and flux-flow instability in high- $T_c$  superconducting films. *Phys. Rev. B* **58**, 11185–11188 (1998). URL <https://link.aps.org/doi/10.1103/PhysRevB.58.11185>.
- [25] Tsen, A. W. *et al.* Nature of the quantum metal in a two-dimensional crystalline superconductor. *Nature Physics* **12**, 208–212 (2016). URL <https://doi.org/10.1038/nphys3579>.